



HAL
open science

Interface coupling method for the global–local analysis of heterogeneous models: A second-order homogenization-based strategy

Maxence Wangermez, Olivier Allix, Pierre-Alain Guidault, Oana Alexandra Ciobanu, Christian Rey

► To cite this version:

Maxence Wangermez, Olivier Allix, Pierre-Alain Guidault, Oana Alexandra Ciobanu, Christian Rey. Interface coupling method for the global–local analysis of heterogeneous models: A second-order homogenization-based strategy. *Computer Methods in Applied Mechanics and Engineering*, 2020, 365, pp.113032. 10.1016/j.cma.2020.113032 . hal-02544212

HAL Id: hal-02544212

<https://hal.science/hal-02544212>

Submitted on 20 May 2022

HAL is a multi-disciplinary open access archive for the deposit and dissemination of scientific research documents, whether they are published or not. The documents may come from teaching and research institutions in France or abroad, or from public or private research centers.

L'archive ouverte pluridisciplinaire **HAL**, est destinée au dépôt et à la diffusion de documents scientifiques de niveau recherche, publiés ou non, émanant des établissements d'enseignement et de recherche français ou étrangers, des laboratoires publics ou privés.



Distributed under a Creative Commons Attribution - NonCommercial 4.0 International License

Interface coupling method for the global-local analysis of heterogeneous models: a second-order homogenization-based strategy

Maxence Wangermez^{a,b}, Olivier Allix^a, Pierre-Alain Guidault^a, Oana Ciobanu^b, Christian Rey^b

^a *Université Paris-Saclay, ENS Paris-Saclay, CNRS, LMT - Laboratoire de Mécanique et Technologie, 94235, Cachan, France.*

^b *Safran Tech, Modelling & Simulation, Rue des Jeunes Bois, Châteaufort, 78114 Magny-Les-Hameaux, France.*

Abstract

This paper proposes a coupling strategy between a homogeneous **macroscopic** description of a structure and a description at a lower scale of some local details. In order to facilitate its implementation in industrial software, an interface coupling technique using a separation between micro and macro quantities of the unknowns is proposed. The approach leads to local solutions equivalent to those that would be obtained by second-order homogenization techniques. Its interest is that it does not require neither the construction of a second-order homogenized model nor a localization stage. The approach is validated against direct **numerical simulations at microscopic scale** on periodic structures under uniform and linear macroscopic strains loads.

Keywords: interface coupling, **non-compatible models**, zooming technique, heterogeneous media, second-order homogenization

1. Introduction

Unlike metallic structures, composite materials have a tendency to suffer from manufacturing anomalies such as excessive porosities or premature phase debonding straight out of the mold. Composite being very damage-tolerant, these anomalies may or may not affect in-service performance. Therefore a number of 3D measurement techniques, such as ultrasound scanning and X-ray tomography, have been developed to characterize them and ultimately capture their morphology. From there, computational assessment of the mechanical performance may be achieved by introducing the generated morphology of the anomaly within an otherwise virgin material.

Given the relative size of manufacturing anomalies — typically between microns and a few micrometers at most — they are usually best represented at the mesoscale, i.e. the scale of the plies in laminates or that of the weaving pattern in woven composites. However since industrial systems are more commonly computed at the macroscale, where all materials are considered homogeneous, some sort of multi-scale seam must be devised to connect the mesoscale anomalous region with the rest of the structure. In other words, engineers are interested in inserting a local mesoscale detail within a predefined finite elements macro-model of a reference structure and predict its effect on the overall mechanical performances. **Figure 1** illustrates these types of problems: described at a full micro-scale (**Figure 1a**), a full macro-scale (**Figure 1b**) and a micro-scale detail embedded in a macro-scale model (**Figure 1c**).

The goal is to recover from a macro-micro coupling of **non-compatible models** (**Figure 1c**) a solution as close as possible to the full reference solution (**Figure 1a**) inside the zone of interest. In this work, the localization of the zone of interest is chosen *a priori*, but it could be determined, for example, by a criterion based on *a posteriori* error estimations, as in the works of [36]. The main issue associated with the introduction of the local detail within the macro-model is the definition of a proper coupling between the two models in order to transfer the relevant macroscopic “information” along with the definition of the complementary microscopic assumptions. This leads to several difficulties regarding the choice of the macroscopic/homogenized model as well as the way to couple models described at different scales, and with different finite element mesh sizes. **The proposed coupling technique is developed in the scope of non-intrusive implementations. It makes use only of quantities, data and functionalities that are available in legacy and commercial codes. That is why, following [19, 15], the proposed coupling technique makes use only of interface quantities. The present article focuses on the coupling choice. The non-intrusive resolution of a coupled problem illustrated in Figure 1c will be detailed in a forthcoming paper.**

In order to clarify the main issue regarding the coupling of **two non-compatible models**, the well established framework of the computational homogenization has been chosen, as it is the basis of numerous multi-scale approaches [41, 34, 43]. One of the most popular computational frameworks associated with it is the FE^2 method [17]. Nevertheless, being based on the first-order theory of homogeniza-

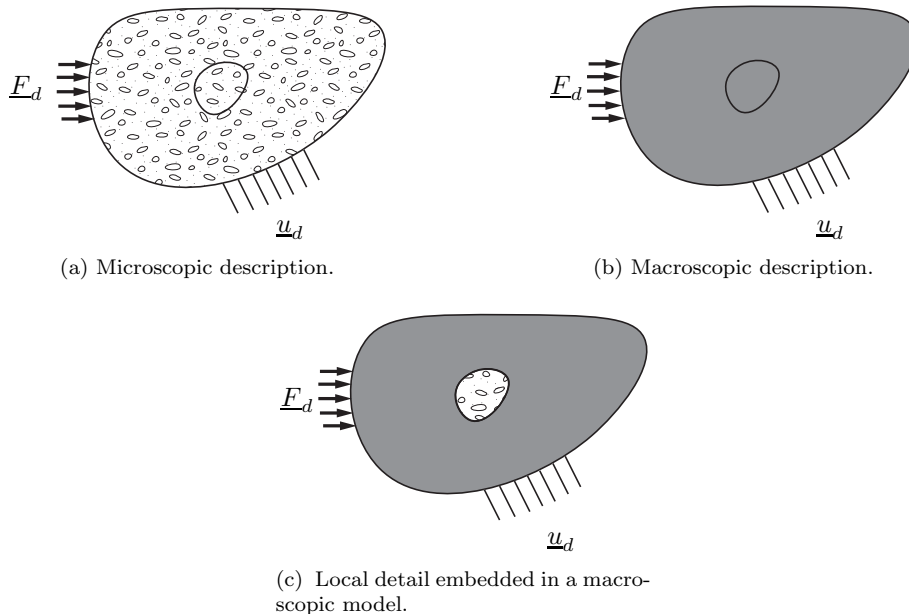


Figure 1: Three various descriptions at different scales of a heterogeneous material structure under prescribed boundary conditions.

tion, this scheme does not introduce size effects of the so-called Representative Volume Element (RVE). To overcome this, several methodologies, for instance based on generalized continua [18, 16, 47, 37, 27] or on numerical filter-based schemes [48, 49, 44] have been proposed. In [27], the authors proposed a two-scale computational framework with the major advantage of treating the RVE as a classical continuum by prescribing boundary conditions. This second-order computational homogenization approach takes into account the gradient effect of the macroscopic solution and hence the effect of the size of the RVE. That is why, in this paper, the considered reference scheme is the second-order computational homogenization one. Compared to the first-order theory, the second-order framework leads to more precise solutions. Let us note that, this framework was extended to deal with thin sheets in [12] and with post-localization aspects in the case of finite strain or damage in [6].

In this paper, in order to directly obtain a solution similar to the one given by a two-step homogenization procedure, an **non-conforming** interface coupling technique is proposed. It allows reducing the incompatibility error between the heterogeneous microscopic (local) model and a first-order homogenized (global) model, representative of the macroscopic behavior of the structure. Its interest is that it does not require neither the construction of a second-order homogenized model nor any post-localization stage. The method bears some relations with the concurrent multi-scale scheme, based on mixed interface coupling, pro-

posed for parallel computing in [33] and further developed in [22] in the case of cracking, and in [39] in the case of delamination and buckling. **The common point is the treatment of interface quantities as variables with a high mechanical content. More precisely, the same micro-macro scale separation and description of interface quantities are used.**

The paper is organized as follows. In **Section 2**, the limitations of a classical coupling approach for compatible models, in the case depicted in **Figure 1c**, are discussed on the basis of a typical example. In **Section 3**, the main principle of second-order homogenization is recalled. In **Section 4**, the Boundary Value Problem within the framework of the Second-Order Computational Homogenization applied on a periodic **medium** is adapted in a multi-scale interface displacement way. In **Section 5**, the coupling conditions between a macro-scale and a micro-scale model are discussed and two numerical examples are given to support the proposal. The conclusions are given in **Section 6**, along with different further research directions based on the obtained results and the long term objectives of the paper.

2. Toy examples and limitations of a classical coupling technique

2.1. Definition of the toy examples

In order to clearly capture the problematic addressed in this paper, a set of 2D finite element structural mechanical problems under linear elasticity assumptions is proposed. The construction of each further discussed example is based on the repetition of a 2D unit cell whose Hookean tensor is denoted by $\mathbf{K}_{\mathcal{L}}$ (linear isotropic elasticity). A reference computational mesh is made of a unit cell repeated a specified number of times, as for example the 5 by 5 unit cells mesh described in **Figure 2a** which corresponds to the full micro-scale problem from **Figure 1a**. Then, the coupled problem is defined over a mesh similar to

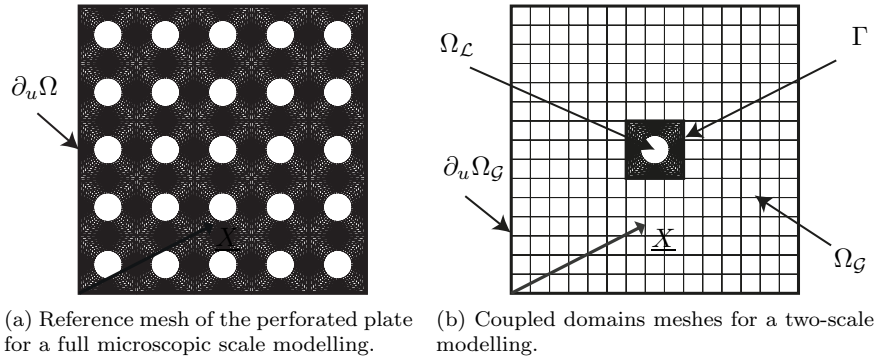


Figure 2: Domains and meshes of a perforated plate.

the one from **Figure 2b**, which corresponds to the problem seen on **Figure 1c**. The central part $\Omega_{\mathcal{L}}$, considered as the local substructure is constituted of a

single (or several) unit cell(s) identical to the one used for the reference problem with the same material properties (Hookean tensor $\mathbf{K}_{\mathcal{L}}$). The external part $\Omega_{\mathcal{G}}$ stands for the global substructure and is modelled by the unit cell effective proprieties $\mathbf{K}_{\mathcal{G}} = \mathbf{K}_{\mathcal{L}}^H$, where $\mathbf{K}_{\mathcal{L}}^H$ is the first-order homogenized behavior of one unit cell under periodicity assumption.

The coupling interface between the global and the local substructures is denoted by Γ . Here, the two substructures are geometrically conforming but their meshes do not necessary match along the coupling surface Γ . In other words, the elements of the two substructures are not cut by Γ and the coupling interface is aligned with the edges of the elements in both substructures. The coupling of non-conforming geometries will be addressed in future works. Interested readers can refer to [8, 23] for recent global-local coupling techniques of conforming and non-conforming geometries.

2.2. Limitations of a classical coupling technique in the case of non-compatible models

Let us consider two examples with different loading cases over the two models shown in **Figure 2**. In these examples, the unit cell is representative of a perforated plate sample. Its size l is 2 mm, it is supposed to be linearly elastic and isotropic and characterized by the Young's Modulus $E = 210$ GPa and the Poisson's ratio $\nu = 0.3$. The homogenized behavior corresponding to the unit cell, as obtained by the classical first-order homogenization is characterized by the following elastic constants: the Young's modulus $E_1 = E_2 = 130.2$ GPa, the Poisson's ratios $\nu_{12} = \nu_{21} = 0.27$ and the shear modulus $G_{12} = 39.8$ GPa.

For the first example, the loading case is intended to impose a uniform macroscopic strain state over the considered domains whereas, in the second example, a linearly varying macroscopic strain state is imposed over the domains. The macroscopic states are prescribed by the same Dirichlet boundary conditions on the outer boundary of the reference problem **Figure 2a** and the coupled problem **Figure 2b**. They are detailed in **Section 5.1**, but not crucial for the well understanding of this section.

A wide range of techniques could be used in order to deal with the coupling of local details inserted in the global domain. For instance, recent developments aim at coupling substructures described by advanced discretization techniques using sophisticated Mortar [14, 11] or Nitsche [13, 1, 35, 40, 7] coupling techniques. Here, in order to deal with the classical finite element discretization and the non-matching grids of the coupled problem, the continuity of interface displacements and equilibrium of forces are ensured in a weak sense, with a *Mortar* finite element formulation with Lagrange Multipliers [31, 3, 4]. The space of Lagrange Multipliers is taken as the trace along the coupling interface of the global-side basis functions. In the following, the notion of "classical coupling" refers to this particular *Mortar* finite element formulation.

To compare the solutions $\underline{u}_{\text{ref}}$ and $\underline{u}_{\mathcal{L}}$ given respectively by the reference problem and by the coupled problem within the local domain $\Omega_{\mathcal{L}}$, an error e_{E} is

defined on each finite element E such as:

$$e_E = \frac{\|u_{\mathcal{L}} - u_{\text{ref}}\|_{E, \mathbf{K}_{\mathcal{L}}}}{\|u_{\text{ref}}\|_{\Omega_{\mathcal{L}}, \mathbf{K}_{\mathcal{L}}}} \quad (1)$$

with the following **energy norm**:

$$\|u_{\mathcal{L}} - u_{\text{ref}}\|_{E, \mathbf{K}_{\mathcal{L}}}^2 = \frac{1}{2 \text{meas}(E)} \int_E \boldsymbol{\varepsilon}(u_{\mathcal{L}} - u_{\text{ref}}) : \mathbf{K}_{\mathcal{L}} : \boldsymbol{\varepsilon}(u_{\mathcal{L}} - u_{\text{ref}}) \, d\Omega$$

where $\text{meas}(E)$ is the surface area of the finite element E .

The error maps for four different meshes of $\Omega_{\mathcal{G}}$ are shown in **Figure 3** according to each loading case. The maps are interpreted as follows: the lower the error, the closer the local solution of the coupled problem is to the reference. As the colormap is truncated after **25%**, the elements of the maps that are displayed in **red** reach an error equal or greater than **25%**. In **Figure 3**, along with each error map, two significant quantities are provided: the maximum value of the error $e_E^{\text{max}} = \max_{E \in \Omega_{\mathcal{L}}}(e_E)$ and the mean value of the error over all the n_E elements of the local model $e_E^{\text{mean}} = 1/n_E \times \sum_{E \in \Omega_{\mathcal{L}}}(e_E)$.

According to **Figure 3**, in both examples, the error decreases with the global mesh size. The lowest error is obtained for the finest global mesh. Thus, it appears that, in both examples, the coupled problem is not equivalent to the reference one. Indeed, whatever the meshes refinements, even with matching grids, an error is made. Moreover, the quality of the solution of the coupled problem is dependent of the discretization.

Therefore, the classical coupling is not adapted to couple different models of heterogeneous structures. The reason is not associated with the use of the *Mortar* approach, which is a generic and effective method for coupling incompatible meshes, but comes from the fact that the problem here lies with the coupling of non-compatible models.

Based on this observation, a new coupling technique which aims to avoid these problems is proposed in the following sections.

3. Main features of the second-order homogenization approach.

In this section, the main features of the second-order homogenization approach are recalled. The interested reader may especially study the works by **Kouznetsova et al.** [30, 27] to have a full description of the method in the finite strain setting.

The basis of second-order periodic homogenization starts by considering the Taylor expansion around a point \underline{X}_c of a finite material vector $\Delta \underline{x}$ in the current configuration at the second-order complemented by a micro-fluctuation \underline{w} :

$$\Delta \underline{x} = \mathbf{F}_M \cdot \Delta \underline{X} + \frac{1}{2} \mathbf{G}_M : \Delta \underline{X} \otimes \Delta \underline{X} + \underline{w}(\Delta \underline{X}) \quad (2)$$

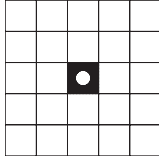
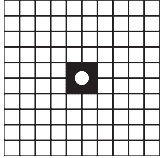
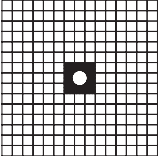
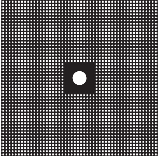
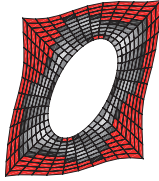
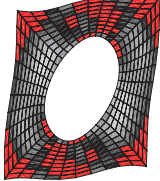
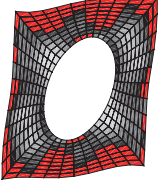
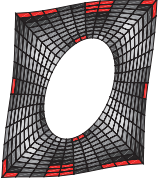
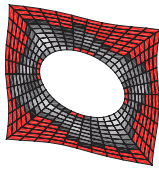
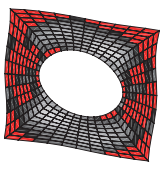
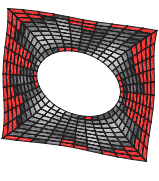
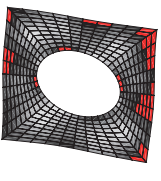
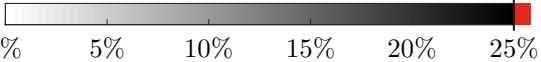
Mesher				
Example 1 uniform macro- strain				
max. error mean error	$e_E^{max} = 69\%$ $e_E^{mean} = 26\%$	$e_E^{max} = 59\%$ $e_E^{mean} = 20\%$	$e_E^{max} = 55\%$ $e_E^{mean} = 20\%$	$e_E^{max} = 31\%$ $e_E^{mean} = 15\%$
Example 2 linear macro- strain				
max. error mean error	$e_E^{max} = 75\%$ $e_E^{mean} = 26\%$	$e_E^{max} = 67\%$ $e_E^{mean} = 21\%$	$e_E^{max} = 60\%$ $e_E^{mean} = 21\%$	$e_E^{max} = 35\%$ $e_E^{mean} = 15\%$
truncated colormap	 0% 5% 10% 15% 20% 25%			

Figure 3: Distribution of local error for four global meshes and two loading cases.

where: \underline{X}_C is the geometrical center of the RVE, $\Delta \underline{x} = \underline{x} - \underline{x}_c$, $\Delta \underline{X} = \underline{X} - \underline{X}_c$. $\mathbf{F}_M = \frac{\partial \phi(\underline{X}_c)}{\partial \underline{X}}$ and $\mathbf{G}_M = \frac{\partial}{\partial \underline{X}} \left(\frac{\partial \phi(\underline{X}_c)}{\partial \underline{X}} \right)$ are respectively second and third-order tensors. Let us note that this definition of \mathbf{G}_M is also used in [38] where the first index i of $G_{M_{ijk}}$ denotes the spatial component. In comparison with the convention taken in [29], the first two indices of $G_{M_{ijk}}$ are inverted. Denoting $\underline{u}_C = \underline{x}_C - \underline{X}_C$, this expression leads to the following one in terms of displac-

ments.

$$\underline{u} = \underline{x} - \underline{X} = \underline{u}_C + \underbrace{(\mathbf{F}_M - \mathbf{I}_d) \cdot \Delta \underline{X} + \frac{1}{2} \mathbf{G}_M : \Delta \underline{X} \otimes \Delta \underline{X}}_{=\underline{u}^M} + \underline{w}(\Delta \underline{X}) \quad (3)$$

In equation (3), \underline{u}^M corresponds to the macroscopic displacements. Following [27, 38], the macroscopic first and second-order gradients are defined as follows:

$$\left\{ \begin{array}{l} \mathbf{F}_M = \frac{1}{V} \int_{\Omega_{RVE}} \mathbf{F}_m \, d\Omega \\ \mathbf{G}_M \cdot \mathbf{J} + \frac{1}{2} \mathbf{G}_M : \mathbf{J} \otimes \mathbf{I}_d = \int_{\partial\Omega_{RVE}} \underline{x} \otimes \Delta \underline{X} \otimes \underline{N} \, d\Gamma \end{array} \right. \quad (4)$$

where \underline{N} is the outward unit normal of the RVE, $\mathbf{J} = \int_{\Omega_{RVE}} \Delta \underline{X} \otimes \Delta \underline{X} \, d\Omega$ is the second moment of volume of the undeformed RVE at point \underline{X}_C and \mathbf{F}_m the microstructural deformation gradient tensor. These relations hold only if \underline{X}_C is the geometric center of the undeformed RVE, i.e. $\int_{\Omega_{RVE}} \underline{X} \, d\Omega = 0$.

In the framework of the second-order homogenization, these relations are used to set up a generalized macroscopic relation linking the average stress and higher-order stress tensors to the first and second gradient of the transformation. Then, using a nested two-scale approach of FE² type [17] but adapted to a second-order description, it is possible to simulate the response of the structure with a refined macroscopic description taking into account gradient effect and to get the associated local response [16, 28]. **The approach taken here is different. Starting from (4), explicit coupling relationships are defined for the interface quantities between the macro and micro models.**

4. Equivalent kinematic admissibility on interface displacements

In the computational homogenization context, the bond between micro and macro descriptions is made by the Boundary Value Problem (BVP). The aim of this section is to determine the explicit relations that link the macroscopic and the microscopic scales on one RVE with an interface micro-macro description of the BVP kinematic admissibility. **From the experience earned from DDM approaches [33, 22, 39], we have decided to choose, as independent quantities, some pertinent averages of the interface displacements. Different aspects of this choice are further discussed.** For the sake of convenience, the approach is detailed for 2D cases and the differences with 3D cases will be mentioned at the end of **Section 4.3**.

4.1. Interface displacements conditions to be satisfied.

The two averaging properties (4) lead to the following kinematic conditions on the fluctuation \underline{w} :

$$\left\{ \begin{array}{l} \int_{\partial\Omega_{RVE}} \underline{w}(\underline{X}_C, \underline{X}) \otimes \underline{N}(\underline{X}) \, d\Gamma = 0 \\ \int_{\partial\Omega_{RVE}} \underline{w}(\underline{X}_C, \underline{X}) \otimes \Delta \underline{X} \otimes \underline{N}(\underline{X}) \, d\Gamma = 0 \end{array} \right. \quad (5)$$

In the first-order homogenization framework, only the first equation of (5) is to be satisfied. Widespread hypotheses to fulfill equations (5) are *kinematic uniform boundary condition* (KUBC), *static uniform boundary condition* (SUBC) or *periodic boundary condition* (PBC). One can refer for example to [46, 25] for more details about the implications of these hypotheses.

In the second-order homogenization framework, the two equations of (5) have to be satisfied. One can refer for example to [27, 24] for more details about extensions of PBC, KUBC and SUBC to second-order homogenization.

Here, the PBC has been chosen because, this assumption gives the most reasonable estimate of the overall response of the RVE [45], as compared with the KUBC which gives an upper-bound estimation and the SUBC which gives a lower-bound estimation. Moreover, the local field of interest is often of higher quality. This is still the case even when the periodicity of the RVE geometry is not strictly satisfied, as shown in [42].

In order to satisfy equation (5), the external boundary $\partial\Omega_{RVE}$ of the RVE can be split into basic faces γ such as, in 2D cases: $\partial\Omega_{RVE} = \bigcup_{\gamma \in \{d,r,t,l\}} \gamma$ where d, r, t, l correspond respectively to the down, right, top and left faces of the RVE described on **Figure 4**.

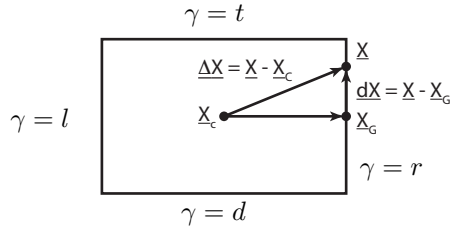


Figure 4: Two-dimensional illustration of the interface position $d\underline{X}$ expressed from the RVE center \underline{X}_C and \underline{X}_G the centroid of the interface r .

For a parallelepiped RVE, one can check that the conditions (5) are fulfilled for any \underline{w} such that:

$$\left\{ \begin{array}{ll} \underline{w}(\underline{X}_C, \underline{X}) & \text{periodic} \\ \int_{\gamma} \underline{w}(\underline{X}_C, \underline{X}) d\Gamma = 0, & \text{for any RVE faces } \gamma \end{array} \right. \quad (6)$$

Different ways to fulfill these equations have been proposed in the literature. For example, in [26, 38], relations (6) are implemented in a FE framework by means of displacement constraints between degrees of freedom in boundary nodes. In [24], equations (5) are directly satisfied by means of a general multiple constraints approach. In this paper devoted to the multi-scale non-compatible coupling, the RVE boundary displacements are split in a multi-scale way and relations are given on each scale.

4.2. *A micro-macro description of the transmission conditions for an interface.*

In order to identify a macroscopic basis consistent with the problem being addressed, let us express, for \underline{X} on any face γ , the boundary displacements \underline{W}_γ of the RVE (see **Figure 4**):

$$\underline{W}_\gamma = \underbrace{\underline{u}_G^* + (\mathbf{F}_M - \mathbf{I}_d) \cdot d\underline{X} + \mathbf{G}_M : \Delta\underline{X}_G \otimes d\underline{X} + \frac{1}{2}\mathbf{G}_M : d\underline{X} \otimes d\underline{X} + w}_{\underline{W}_\gamma^M} \quad (7)$$

with $\Delta\underline{X}_G = \underline{X}_G - \underline{X}_C$, as seen on **Figure 4** and:

$$\underline{u}_G^*(\underline{X}_G, \underline{X}_C) = \underline{u}_C(\underline{X}_C) + (\mathbf{F}_M - \mathbf{I}_d) \cdot \Delta\underline{X}_G + \frac{1}{2}\mathbf{G}_M : \Delta\underline{X}_G \otimes \Delta\underline{X}_G$$

According to (7), the displacement on one face is linear and quadratic in $d\underline{X}$ and depends on the fluctuation w . Thus, on every face γ , a scale separation can be made and equations (6) and (7) can be adapted to satisfy the BVP in a multi-scale interface displacement way. To this end, a macroscopic basis can be defined in order to extract the mean parts, the linear parts and the quadratic parts of the interface displacement \underline{W}_γ of γ . In this work, the general framework proposed in [32] to extract these macroscopic components is followed and partially developed in **Appendix A**.

4.3. *Quadratic macro-components for a second-order interface kinematics*

The projectors onto the macro-basis mentioned above are defined such as $\mathbf{\Pi}_\gamma^T(\underline{W}_\gamma) = \underline{W}_\gamma^T$ extracts the mean (translation) parts of the interface displacement \underline{W}_γ , the projector $\mathbf{\Pi}_\gamma^L(\underline{W}_\gamma) = \underline{W}_\gamma^L$ extracts its linear (rotation/extension) parts and $\mathbf{\Pi}_\gamma^Q(\underline{W}_\gamma) = \underline{W}_\gamma^Q$ extracts its quadratic parts. On one interface γ , each projector is built orthogonal to the others in the sense of the scalar product defined in the **Appendix A** and the macroscopic parts of the interface displacement $\mathbf{\Pi}_\gamma^M(\underline{W}_\gamma)$ are defined by:

$$\mathbf{\Pi}_\gamma^M(\underline{W}_\gamma) = \underbrace{\mathbf{\Pi}_\gamma^T(\underline{W}_\gamma)}_{\text{constant}} + \underbrace{\mathbf{\Pi}_\gamma^L(\underline{W}_\gamma)}_{\text{linear in } d\underline{X}} + \underbrace{\mathbf{\Pi}_\gamma^Q(\underline{W}_\gamma)}_{\text{quadratic in } d\underline{X}} \quad (8)$$

The complementary parts \underline{W}_γ^m are defined by:

$$\underline{W}_\gamma^m = (\mathbf{I} - \mathbf{\Pi}_\gamma^M)(\underline{W}_\gamma) \quad (9)$$

Note that \underline{W}_γ^M and \underline{W}_γ^m are orthogonal in the sense of the chosen scalar product.

4.4. *Proposition of micro-macro coupling conditions*

In 2D, the external boundary $\partial\Omega_{RVE}$ of the RVE is made of 4 basic faces, thus, one has to determine the 12 homogenization macroscopic quantities of \underline{u}_C , \mathbf{F}_M and \mathbf{G}_M from the 24 interface macro-components \underline{W}_γ^T , \underline{W}_γ^L and \underline{W}_γ^Q for $\gamma \in \{d, r, t, l\}$. Consequently, in order to satisfy the kinematic macroscopic

state of the BVP, 12 constraints have to be determined on the interface macro-components according to the values of \underline{u}_C , \mathbf{F}_M and \mathbf{G}_M and 12 additional compatibility constraints between the interface macro-components themselves have to be imposed.

In order to satisfy the second relation of equation (6), on each interface γ , the translation macro-components are imposed such as:

$$\underline{W}_{\gamma}^T = \underline{u}_{G_{\gamma}}^* S_{\gamma} + \frac{1}{2} \mathbf{G}_M : \mathbf{M}_{G_{\gamma}} \quad (10)$$

with the surface of γ denoted by S_{γ} and the matrix of the products of moment of area of the undeformed interface γ at point $\underline{X}_{G_{\gamma}}$ denoted by $\mathbf{M}_{G_{\gamma}} = \int_{\gamma} d\underline{X} \otimes d\underline{X} d\Omega$. From Appendix B, it can be deduced that the 8 translation macro-components are related to only 10 out of the 12 homogenization macroscopic quantities. Consequently, 4 additional equations are required to totally defined the 12 homogenization macroscopic quantities.

The linear macro-components are related to 6 homogenized macroscopic quantities: 4 quantities associated to \mathbf{F}_M and G_{xxy}^M and G_{yxy}^M . The components G_{xxy}^M and G_{yxy}^M are only linked to the linear macro-components. As the fluctuation \underline{w} contains linear parts on the interfaces (i.e. the linear parts of the local and global interface displacements are different), the linear macro-components cannot be explicitly imposed because \underline{w} is not known *a priori*. Nevertheless, as \underline{w} is periodic, the jump of linear macro-components can be imposed such as :

$$\underline{W}_{\gamma^+}^L - \underline{W}_{\gamma^-}^L = S_{\gamma} \mathbf{G}_M : \underline{N}_{\gamma}^+ \otimes d\underline{X} \quad (11)$$

where each face $\gamma^+ \in \{t, r\}$ is facing the opposite face $\gamma^- \in \{d, l\}$ (see Figure 5). In this way, equation (11) is compatible with the first relation of (6) and involves only two macroscopic components out of the four remaining unknowns: G_{xxy}^M and G_{yxy}^M . The four relations given by equation (11) are compatible with the second-order kinematics but only two are necessary to determine the state of macroscopic deformation of the unit cell (see the expressions of G_{xxy}^M and G_{yxy}^M in Appendix B).

Thus, two additional equations are still required to totally define the 12 homogenization macroscopic quantities. Different options can be made in order to close the system (10)-(11). For instance, as the fluctuation solution \underline{w} is supposed to be null on the RVE corners due to the periodic consideration, the full field displacement can be imposed in one corner A :

$$\underline{u}(A) = \underline{u}^M(A) \quad (12)$$

This condition is interesting as it does not involve the quadratic interface macro-components which needs a quadratic mesh to be exactly represented. However, in a general case with a not purely second-order macroscopic solution, this condition would lead to different solution according to the selected corner.

One can prefer a non-local condition to define the last two missing relations, but it would add additional conditions on the interface macro-components,

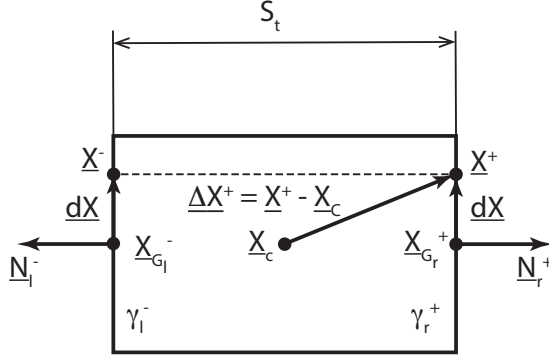


Figure 5: Periodicity notations for a pair of opposite faces on a 2D parallelepiped RVE.

avoided so far. Nevertheless, it would be an improvement for the proposed coupling technique. The search of the “best” non-local conditions for not purely periodic case is still an open question.

In summary, relations (10)-(12) provide the links between the 24 interface macro-components and the macroscopic state defined by the 12 parameters of \underline{u}_C , \mathbf{F}_M and \mathbf{G}_M . As said previously, 12 additional kinematically admissible conditions have to be imposed between the interface macro-components themselves.

From the 12 additional conditions sought, as the problem is solved by FEM, 8 are automatically satisfied by the continuity of the displacement at the RVE corners. Indeed, if the periodic conditions are satisfied by \underline{w} , the fluctuation vanishes on the RVE corners so that the macroscopic parts of the interface displacement (8) are continuous between two contiguous edges of the RVE, even if the interface macro-components are not.

The last 4 compatibility equations sought to define the interface macro-components admissibility arise from the periodicity of the quadratic macro-components between the facing interfaces γ^+/γ^- :

$$\underline{W}_{\gamma^+}^Q - \underline{W}_{\gamma^-}^Q = \underline{0} \quad (13)$$

Finally, in order to completely satisfy the first equation of (6), the microscopic parts of the interface displacement defined by (9) must verify the following condition:

$$\underline{W}_{\gamma^+}^m - \underline{W}_{\gamma^-}^m = \underline{0} \quad (14)$$

To conclude, in order to solve the 2D-BVP with a micro-macro description of boundary relations, the following relations have to be satisfied. On each interface γ , the mean part have to be imposed such as :

$$\underline{W}_{\gamma}^T = \underline{u}_{G_\gamma}^* S_\gamma + \frac{1}{2} \mathbf{G}_M : \mathbf{M}_{G_\gamma}$$

The jump of linear macro-components between pair of interface γ^+/γ^- must be chosen according to the expressions of G_{xxy}^M and G_{yxy}^M given in **Appendix B**, such as:

$$\underline{W}_{\gamma^+}^L - \underline{W}_{\gamma^-}^L = S_\gamma \mathbf{G}_M : \underline{N}_\gamma^+ \otimes d\underline{X}$$

And, on one corner, the full field displacement is imposed such as:

$$\underline{u}(A) = \underline{u}^M(A)$$

Then, periodicity conditions on each pair of interface γ^+/γ^- have to be enforced. The quadratic macro-components have to satisfy:

$$\underline{W}_{\gamma^+}^Q - \underline{W}_{\gamma^-}^Q = \underline{0}$$

and the micro-components have to satisfy:

$$\underline{W}_{\gamma^+}^m - \underline{W}_{\gamma^-}^m = \underline{0}$$

In 3D cases, 30 macroscopic unknowns are involved in the second-order approach: 3 components of the rigid body displacement \underline{u}_c , 9 components of the deformation gradient tensor \mathbf{F}_M and 18 components of the gradient of the gradient deformation \mathbf{G}_M . The external boundary $\partial\Omega_{RVE}$ of the RVE can be split into 6 basic faces γ such as: $\partial\Omega_{RVE} = \bigcup_{\gamma \in \{d,r,t,l,f,b\}} \gamma$ where d, r, t, l, f, b correspond respectively to the down, right, top, left, front and back faces of the RVE. Working with multi-scale interface quantities, 108 interface macro-components arise. Among them, 75 are automatically satisfied by the displacement continuity at the edges of the parallelepipedic RVE. Thus, 33 relations have to be fixed: 30 are fixed by the values of \underline{u}_c , \mathbf{F}_M and \mathbf{G}_M and 3 constraints between interface macro-components. **Therefore, as in the 2D case, half of the conditions on the linear macro-components have to be imposed, according to the expression of the terms of \mathbf{G}_M involved by the linear macro-components. But also, only 3 of the 27 conditions on quadratic macro-components have to be imposed. As previously, this choice has no consequence on the purely second-order macroscopic solution, offering flexibility to the proposed method.**

Remark 1. *In **Appendix B** are given the components of \underline{u}_c , \mathbf{F}_M and \mathbf{G}_M according to the macroscopic interface displacement terms in the particular case of a 2D example. It is interesting to note that they are calculated only with surface integrals and are only dependent on the mean and linear parts of the interface displacement and on the displacement fixed at corner A. Thus, these relations may be seen as an alternative way to compute second-order gradients with surface integrals rather than volume integrals. Note that the definitions of these surface integrals are independent from the mesh discretization.*

Remark 2. *KUBC or SUBC can be satisfied by imposing respectively nullity ($\underline{W}_\gamma^m = \underline{0}$) or freedom conditions on the microscopic components of the interface displacement field on each γ interface instead of the last periodic relation (14):*

$$\underline{W}_{\gamma^+}^m - \underline{W}_{\gamma^-}^m = \underline{0}$$

4.5. Validation of the proposed conditions to solve the BVP

A numerical analysis has been made in order to compare these BVP conditions to the classical ones. In [29], a perfectly periodic perforated plate composed of 3×3 RVEs has been investigated. The same problem is considered here, with the major exception that the small deformation theory is adopted instead of the large deformation one. The solution obtained by imposing relations (10)-(14) is compared to the one obtained using the method suggested in [29]. The solution of [29] was rebuilt by imposing the displacement on the four corners of the RVE, the constraints on the opposite boundaries and the zero-averaged fluctuation along two contiguous boundaries.

The test case is such that the size of the RVE is taken equal to $10\mu m$, the material behavior of the plate is supposed to be linearly elastic and the material parameters are taken such as the Young's modulus E equals 210 GPa and the Poisson's ratio ν equals 0.3.

The plate has been subjected to the same prescribed bending-tension deformation loading as in [29]. Thus, the prescribed macroscopic kinematic quantities are: $F_{xx}^M = 1.1$, $F_{yy}^M = 0.9$ and $G_{yxx}^M = -18\text{mm}^{-1}$, $G_{xxy}^M = G_{xyx}^M = 12\text{mm}^{-1}$, $G_{yyy}^M = -8\text{mm}^{-1}$ and the other components are taken equal to zero.

The **Figure 6** shows the von Mises stress map in the deformed plate for the prescribed loading applied by relations (10)-(14). According to the **energy norm** defined by (1), the difference between the solution obtained by imposing the relations (10)-(14) and the solution obtained by imposing relations from [29] is under $10^{-6}\%$. Thus, validating the proposed relations.

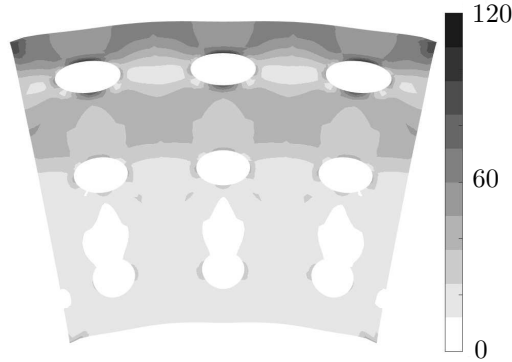


Figure 6: von Mises stress map (in GPa) of the linear elastic deformed plate for a prescribed bending-tension deformation loading, under small deformations hypothesis, computed by relations (10)-(12).

5. Towards a multi-scale global/local strategy for non-compatible models

Let us return to the initial goal of the paper: the coupling of two models representatives of an heterogeneous material at different scales. Let us note that, the same type of question arises in the case of the coupling between a plate and a 3D model for which a different coupling technique also based on homogenization was proposed in [20] and developed in [21]. **Section 2** shows that the classical coupling conditions are too strong to deal with non-compatible models. In this section, a coupling strategy between a first-order homogenized macroscopic (global) model and a micro-structured heterogeneous (local) model is proposed. The method is based on the exchange of interface macroscopic quantities defined in **Section 4.3**. Then, two examples are given to validate the method under uniform macro-strain and linear macro-strain loadings.

The same notations as in **Section 2** are taken: the subscripts \mathcal{L} , \mathcal{G} respectively refer to the local substructure ($\Omega_{\mathcal{L}}$) and the global substructure ($\Omega_{\mathcal{G}}$). As the global substructure is supposed to be the homogenized model of the local substructure, relation (7) becomes :

$$\underline{W}_{\mathcal{L},\gamma}(\underline{X}) = \underline{W}_{\mathcal{G},\gamma}(\underline{X}) + \underline{w} \quad (15)$$

with \underline{w} which satisfy (6).

The coupling relations between the global and the local substructures are built from relations (10)-(14) defined in **Section 4.3**. According to (10), the mean part of interface displacements of the local substructure ($\underline{W}_{\mathcal{L},\gamma}^T$) is taken equal to the one of the global substructure ($\underline{W}_{\mathcal{G},\gamma}^T$) for all the interfaces (in 2D: $\gamma \in \{d, r, t, l\}$ and in 3D: $\gamma \in \{d, r, t, l, f, b\}$):

$$\underline{W}_{\mathcal{L},\gamma}^T = \underline{W}_{\mathcal{G},\gamma}^T \quad (16)$$

Then, according to (11), the jumps of linear parts of interface displacements between the local model and the global model have to satisfy the following relations between pair of interfaces γ^+/γ^- :

$$\underline{W}_{\mathcal{L},\gamma^+}^L - \underline{W}_{\mathcal{L},\gamma^-}^L = \underline{W}_{\mathcal{G},\gamma^+}^L - \underline{W}_{\mathcal{G},\gamma^-}^L \quad (17)$$

And, the displacement continuity is imposed in one corner according to (12) :

$$\underline{u}_{\mathcal{L}}(\underline{A}) = \underline{u}_{\mathcal{G}}(\underline{A}) \quad (18)$$

As we are seeking for the local substructure displacement fields kinematically admissible with a second-order displacement field, the quadratic part of the global and the local displacements must be periodic according to (13). This implies that:

$$\underline{W}_{\mathcal{L},\gamma^+}^Q - \underline{W}_{\mathcal{L},\gamma^-}^Q = \underline{W}_{\mathcal{G},\gamma^+}^Q - \underline{W}_{\mathcal{G},\gamma^-}^Q = \underline{0} \quad (19)$$

This choice may be too restrictive in case of higher than second-order complex loadings because it compels the global and local displacement fields to be kinematically admissible with a second-order displacement field on the interfaces. But, it is a necessary condition for the uniqueness of \mathbf{G}_M on each interface.

To ensure the periodicity hypothesis on the local substructure, the jumps of the microscopic part of the interface displacements are taken periodic:

$$\underline{W}_{\mathcal{L},\gamma^+}^m - \underline{W}_{\mathcal{L},\gamma^-}^m = \underline{W}_{\mathcal{G},\gamma^+}^m - \underline{W}_{\mathcal{G},\gamma^-}^m = \underline{0} \quad (20)$$

Thus, equations (16)-(20) are equivalent to (15) with $\underline{W}_{\mathcal{G},\gamma}$ and $\underline{W}_{\mathcal{L},\gamma}$ kinematically admissible with a second-order displacement field.

In summary, both coupling and periodicity conditions have to be prescribed in order to have a compatible formulation with second order kinematics. The coupling conditions that link the micro-model and the macro-model can be expressed as follows:

- continuity of the mean part of interface displacements at each interface,
- equality of the jumps of the linear parts of the displacements between pairs of interfaces,
- continuity of the full field displacements at one corner.

Then, periodicity conditions are additionally enforced to the quadratic and microscopic parts of interface displacements for the local and global domains.

Kinematic relations (16)-(20) can be imposed, for example, by Lagrange multipliers. The micro-macro separation of the interface quantities makes it possible to deduce the relations between the interface force distributions at the different scales. These relations can be interpreted as dependencies between the models in terms of resultants and moments on each interface.

With the same scale separation as in (8) and (9) the interface force distributions are written according to the following micro-macro formalism:

$$\begin{aligned} \underline{F}_{\mathcal{G},\gamma} &= \underline{F}_{\mathcal{G},\gamma}^T + \underline{F}_{\mathcal{G},\gamma}^L + \underline{F}_{\mathcal{G},\gamma}^Q + \underline{F}_{\mathcal{G},\gamma}^m \\ \underline{F}_{\mathcal{L},\gamma} &= \underline{F}_{\mathcal{L},\gamma}^T + \underline{F}_{\mathcal{L},\gamma}^L + \underline{F}_{\mathcal{L},\gamma}^Q + \underline{F}_{\mathcal{L},\gamma}^m \end{aligned}$$

As developed in **Appendix A**, the microscopic part \underline{F}_{γ}^m and the macroscopic parts \underline{F}_{γ}^T , \underline{F}_{γ}^L and \underline{F}_{γ}^Q of force distribution \underline{F}_{γ} ($= \underline{F}_{\gamma}^T + \underline{F}_{\gamma}^L + \underline{F}_{\gamma}^Q + \underline{F}_{\gamma}^m$) are defined such that the work is uncoupled between scales:

$$(\underline{W}_{\gamma}, \underline{F}_{\gamma})_{\gamma} = (\underline{W}_{\gamma}^T, \underline{F}_{\gamma}^T)_{\gamma} + (\underline{W}_{\gamma}^L, \underline{F}_{\gamma}^L)_{\gamma} + (\underline{W}_{\gamma}^Q, \underline{F}_{\gamma}^Q)_{\gamma} + (\underline{W}_{\gamma}^m, \underline{F}_{\gamma}^m)_{\gamma} \quad (21)$$

with the scalar product given by:

$$(\underline{W}_{\gamma}, \underline{F}_{\gamma})_{\gamma} = \int_{\gamma} \underline{W}_{\gamma} \cdot \underline{F}_{\gamma} \, d\Gamma$$

Thus, the static coupling relations are given by the following relations on each scale:

$$\begin{cases} \underline{F}_{\mathcal{G},\gamma}^T + \underline{F}_{\mathcal{L},\gamma}^T &= \underline{\mathbf{0}} \\ \underline{F}_{\mathcal{G},\gamma}^L + \underline{F}_{\mathcal{L},\gamma}^L &= \underline{\mathbf{0}} \end{cases}$$

and, the following anti-periodic relations are given on pairs of opposite interfaces:

$$\begin{cases} \underline{F}_{\mathcal{G},\gamma^+}^L + \underline{F}_{\mathcal{G},\gamma^-}^L &= \underline{F}_{\mathcal{L},\gamma^+}^L + \underline{F}_{\mathcal{L},\gamma^-}^L &= \underline{\mathbf{0}} \\ \underline{F}_{\mathcal{G},\gamma^+}^Q + \underline{F}_{\mathcal{G},\gamma^-}^Q &= \underline{F}_{\mathcal{L},\gamma^+}^Q + \underline{F}_{\mathcal{L},\gamma^-}^Q &= \underline{\mathbf{0}} \\ \underline{F}_{\mathcal{G},\gamma^+}^m + \underline{F}_{\mathcal{G},\gamma^-}^m &= \underline{F}_{\mathcal{L},\gamma^+}^m + \underline{F}_{\mathcal{L},\gamma^-}^m &= \underline{\mathbf{0}} \end{cases}$$

Due to the micro and macro works uncoupled property (21), it is then possible to show that Hill-Mandel theorem is satisfied for uniform macroscopic deformation at the local model scale. This ensures equality of the macroscopic work in the transition from the global model to the local model.

The details of the associated finite element system are given in **Appendix C**. In the following, the proposed formulation is validated on several numerical examples.

5.1. Numerical validation with first and second-order examples for periodic media

In this section, a pair of theoretical cases highlights the ability of the proposed method **to couple non-compatible models** in the case of the substructured problem shown in **Figure 2**.

The size of one RVE, l is 2 mm. The material itself is linearly elastic and isotropic and characterized by the Young's Modulus $E = 210$ GPa and the Poisson's ratio $\nu = 0.3$.

The homogenized behavior corresponding to the unit cell, as obtained by the classical first-order homogenization under periodicity assumption, is characterized by the following elastic constants: the Young's modulus $E_1 = E_2 = 130.2$ GPa, the Poisson's ratios $\nu_{12} = \nu_{21} = 0.27$ and the shear modulus $G_{12} = 39.8$ GPa.

Example 1. As a first example, the 2D-domains considered in **Section 2** (see **Figure 2**) are subjected to Dirichlet boundary conditions such as a macroscopic uniform strain is prescribed on the considered domains. Then, the displacement prescribed at the external boundary of the domains $\partial_u\Omega$ and $\partial_u\Omega_G$ is:

$$\underline{u}_d = \underline{u}_C + \underline{\varepsilon}_0 \cdot \underline{X} = \begin{bmatrix} 0.05 \\ 0.05 \end{bmatrix} + \begin{bmatrix} 0.002 & 0.01 \\ 0.01 & 0.02 \end{bmatrix} \cdot \underline{X} \quad (22)$$

with \underline{X} the coordinate vector of the structures (see **Figure 2a**). In the case of a homogeneous structure the strain would then be uniform and equal to $\underline{\varepsilon}_0$. The reference solution is presented in **Figure 7**.

The deformation solution of the coupled problem is shown on **Figure 8**. One notes that the displacement is discontinuous at the interface between Ω_G and Ω_L . Indeed, the continuity of the displacement is imposed only on the

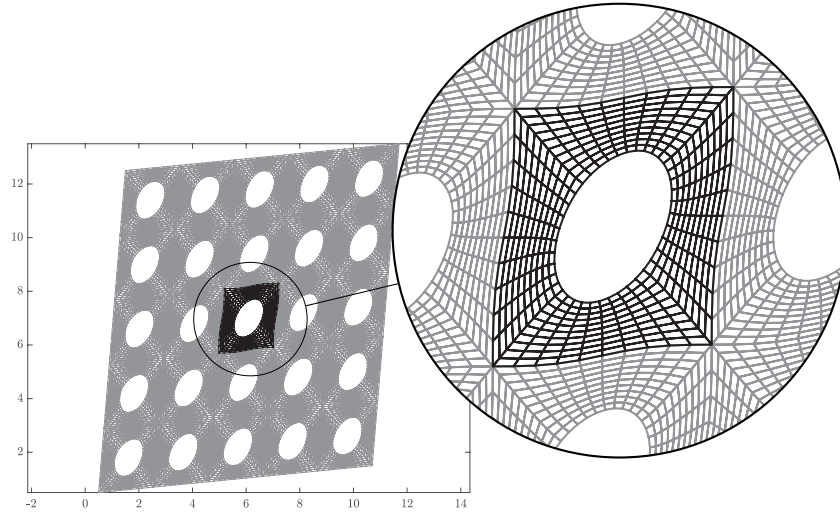


Figure 7: Deformed shape of the reference problem solution under the prescribed uniform macroscopic strain (22).

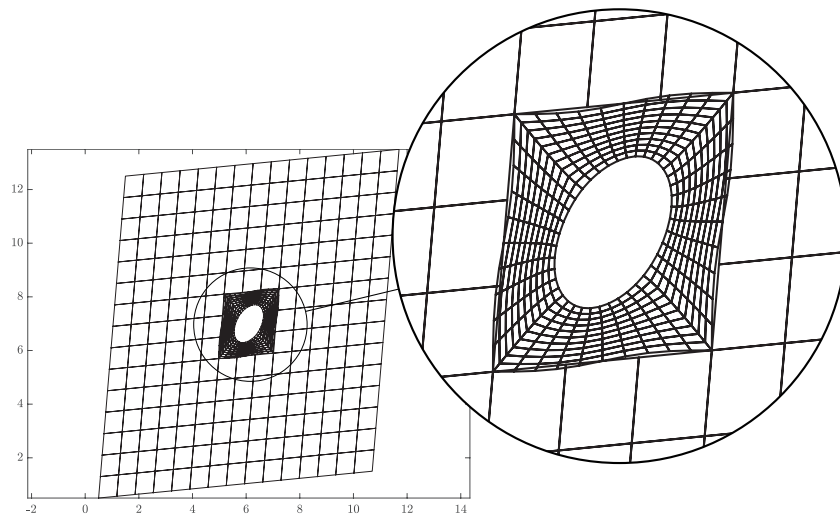


Figure 8: Illustration of the deformed solution for the proposed coupling technique under the prescribed uniform macroscopic strain (22).

mean (translation) components of each interface. Moreover, the displacement solution on $\Omega_{\mathcal{G}}$ corresponds to the one which could have been computed on a full macroscopic computation (**Figure 1b**). The displacement solution on $\Omega_{\mathcal{L}}$ is periodic and matches the solution of the first-order BVP on the RVE under periodic hypothesis.

The stress map of the reference problem solution is shown on **Figure 9a**. It can be noted that, from a macroscopic point of view, the solution is quite uniform throughout the reference structure. And, from a microscopic point of view, the stress is similar from one RVE to another except for some RVEs closed to the outer boundary of the domain. This is due to edge effects that can be observed on the reference solution (see **Remark 3**). The stress map of the coupled problem solution is shown on **Figure 9b**. One can note that the stress on $\Omega_{\mathcal{G}}$ is uniform and consistent with a full homogenized macroscopic computation. The solutions in the zone of interest seems to be very similar with the solution given by the reference problem as discussed hereafter.

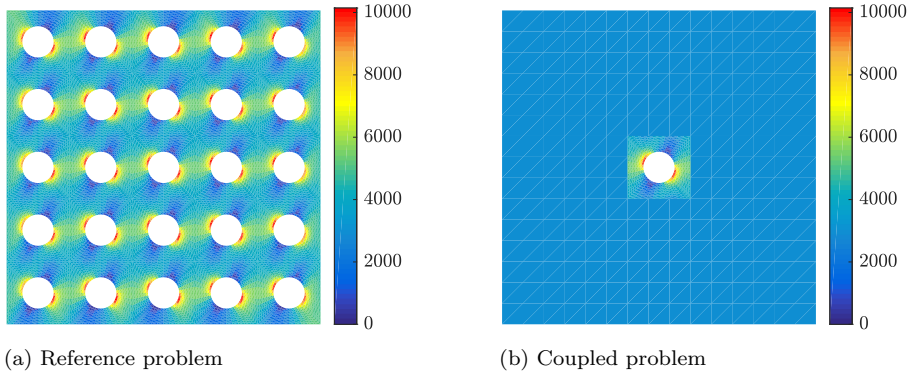


Figure 9: Equivalent von-Mises stress map solutions under a uniform macroscopic strain.

The obtained error map drawn on the warped central RVE between the solutions of the coupled problem and the reference problem is shown in **Figure 10**. The maximum relative energetic error is of 1.56% regardless of the discretization. The improvement is especially significant in comparison with the results obtained with the classical coupling technique which is not designed to deal with non-compatible models in a continuum mechanics way (see **Figure 3**). The error level is much lower with the proposed coupling technique and the solution is independent of the discretization of the global model.

The coupled problem gives the expected results on the local and global substructures as it gives the solution of the full-homogenized model on $\Omega_{\mathcal{G}}$ and the exact solution of the first-order periodic BVP at micro-scale on $\Omega_{\mathcal{L}}$. Indeed, the maximum error value between the solution of the coupled problem on $\Omega_{\mathcal{L}}$ and the exact solution of the first-order periodic BVP on a single RVE is under $1e^{-11}\%$.

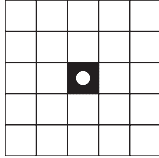
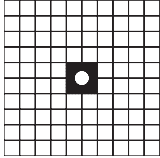
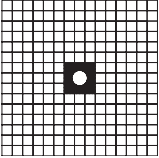
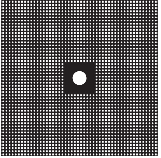
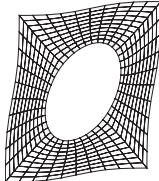
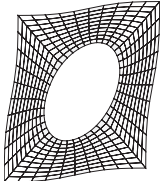
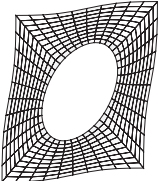
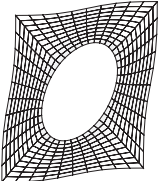
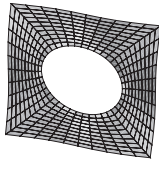
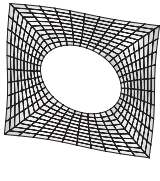
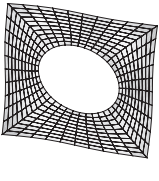
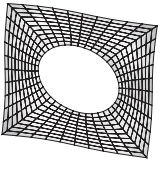
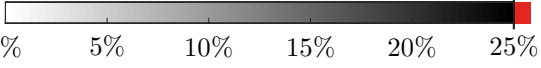
Meshes				
Example 1 uniform macro- strain				
max. error mean error	$e_E^{max} = 1.56\%$ $e_E^{mean} = 0.70\%$	$e_E^{max} = 1.56\%$ $e_E^{mean} = 0.70\%$	$e_E^{max} = 1.56\%$ $e_E^{mean} = 0.70\%$	$e_E^{max} = 1.56\%$ $e_E^{mean} = 0.70\%$
Example 2 linear macro- strain				
max. error mean error	$e_E^{max} = 15.37\%$ $e_E^{mean} = 8.36\%$	$e_E^{max} = 6.77\%$ $e_E^{mean} = 2.73\%$	$e_E^{max} = 6.80\%$ $e_E^{mean} = 2.60\%$	$e_E^{max} = 7.54\%$ $e_E^{mean} = 2.54\%$
colormap	 0% 5% 10% 15% 20% 25%			

Figure 10: Error maps based on the energetic criterion e_E defined on (1) between \underline{u} the displacement solution of coupled problem central unit cell and \underline{u}_{ref} the displacement solution of reference problem central unit cell. Error drawn on the deformed shapes of Ω_C with scale factors.

Remark 3. *One can note that the reference problem is not equivalent to the first-order periodic BVP. Hence, the observed errors ($< 1.56\%$) shown on the map of **Figure 10** can be explained by edge effects. Indeed, in the reference problem, the central RVE is not really periodic because the boundary condition (22) is not compatible with the periodic hypothesis near the outer boundary of the domain $\partial_u \Omega_G$. Thus, the more RVEs compose the domain the more periodic*

will be the displacement on the central RVE.

To convince of this, the average strain $\underline{\varepsilon}_s^M$ with $s \in \{\mathcal{G}, \mathcal{L}, \text{ref}\}$ is defined by: $\underline{\varepsilon}_s^M = (\mathbf{K}_{\mathcal{L}}^H)^{-1} : \underline{\sigma}_s^M$ with the average stress $\underline{\sigma}_s^M$ over the domain Ω_s given by $\underline{\sigma}_s^M = \frac{1}{\text{meas}(\Omega_s)} \int_{\Omega_s} \underline{\sigma}_s d\Omega$ and with $\mathbf{K}_{\mathcal{L}}^H$ the homogenized material behavior of the RVE.

On the coupled problem, in both substructures $\Omega_{\mathcal{G}}$ and $\Omega_{\mathcal{L}}$, the average strain equals the one imposed on the boundary: $\underline{\varepsilon}_{\mathcal{L}}^M = \underline{\varepsilon}_{\mathcal{G}}^M = \underline{\varepsilon}_0$. On the reference problem the average strain $\underline{\varepsilon}_{\text{ref}}^M$ over the central RVE gives:

$$\underline{\varepsilon}_{\text{ref}}^M = \begin{bmatrix} 0.0020002 & 0.010152 \\ 0.010152 & 0.020039 \end{bmatrix}$$

which is different from the prescribed $\underline{\varepsilon}_0$ given in (22).

Example 2. In the second example, the same structures as those given in **Figure 2** are subjected to a linearly varying macro-strain. The following displacement is then applied on the outer edges of Ω and $\Omega_{\mathcal{G}}$:

$$\underline{u}_d = (\mathbf{F}_0 - \mathbf{I}_d) \cdot \underline{X} + \frac{1}{2} \mathbf{G}_0 : \underline{X} \otimes \underline{X} \quad (23)$$

with $F_0^{xx} = 1.002$ and $F_0^{yy} = 0.998$ the non-null components of \mathbf{F}_0 . The non-null components of the prescribed \mathbf{G}_0 are $G_0^{xxy} = 2\text{E}^{-3} \text{ mm}^{-1}$, $G_0^{yyx} = 4\text{E}^{-4} \text{ mm}^{-1}$, $G_0^{xyy} = -7.7\text{E}^{-4} \text{ mm}^{-1}$ and $G_0^{yxx} = -3.9\text{E}^{-3} \text{ mm}^{-1}$. They are chosen such that $\text{div}(\mathbf{K}_{\mathcal{L}}^H : \underline{\varepsilon}(\underline{u}_d)) = \underline{0}$. Such a boundary condition prescribes a linearly varying macro-strain on the whole domain of a homogeneous material.

The stress map solution of the reference problem is shown on **Figure 11a**. An evolution of the macroscopic stress at the scale of the structure is clearly visible since the stress increases between the RVE at the bottom left corner and the RVE at the top right corner. On the coupled problem, the macroscopic gradient of stress is also visible on the global substructure. As the maximum value of the reference problem is related to the top right hand corner RVE solution whereas the maximum value of the coupled problem is related to the central RVE, the color scale has been arranged to facilitate the comparison of the von-Mises stress in the zone of interest (the central RVE). In this zone, the solutions for the two models seem to be very similar as discussed hereafter.

The **Figure 10** highlights the local difference between the solutions of the coupled problem and the reference problem with the local error defined by (1). The errors maps show that the reference problem is quite well approximated compared with classical techniques: the maximum relative error is between 5 and 40 times smaller than the one found with the coupling technique for compatible models.

In this second example, it can be noticed that the error is a little higher than in the first example. In addition, their trends follow those of the errors of **Figure 3**. These errors can be explained by three different reasons.

The first one is that, in the same way as in the first example, the boundary conditions of the reference and coupled problems are not identical. Indeed,

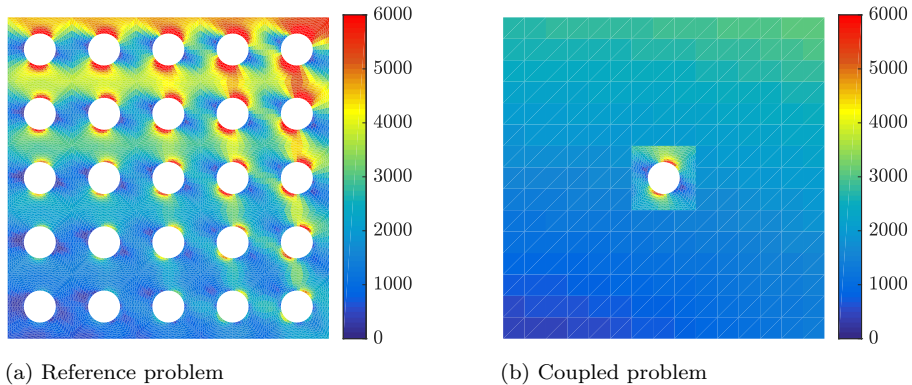


Figure 11: Equivalent von-Mises stress map solutions under a linearly varying macroscopic strain.

as mentioned in **Remark 3**, the boundary conditions on the reference problem satisfy full field Dirichlet conditions whereas on the coupled problem, the Dirichlet conditions are applied on the homogenized substructure. In other words, on the reference problem, the micro-displacement is imposed to vanish on the outer edges of the reference structure while on the coupled problem, the micro-displacement is implicitly supposed to be periodic.

A second source of error comes from the linear interpolation of the finite element shape functions used to compute the solutions. Indeed, as a macroscopic linear strain is enforced, it corresponds to a quadratic displacement on the global subdomain Ω_G . This quadratic displacement is then not exactly computed with a linear mesh. This explains the error variation similar to the one in **Figure 3**.

A third source of errors comes from the material behavior of the global substructure. Indeed, the micro-structured RVE is not well represented by a first-order periodic homogenized material behavior because, in this case, the strain variation is not negligible according to the size of the RVE. Therefore, the macroscopic behavior of the RVE is not well represented by the used first-order periodic homogenized behavior.

A major benefit from this technique is that, due to the mechanical sense of the macro-basis, the proposed coupling technique is nearly insensible to the discretization. Indeed, the shared macroscopic quantities are defined before any discretization. No matter how coarse are the meshes, if they can describe the macroscopic quantities, the technique is valid. **This last point partially illustrates the reason why, in example 2, for the coarsest global refinement, there is a higher error. Indeed, the linear global mesh only offers a linear interpolation of the displacement field on the coupling interface. This discretization does not provide a proper description of the solution sought in the global domain.**

Up to now, the local substructure corresponded to a single RVE. In the following section, different sizes and patterns of the local substructure Ω_L are analyzed.

5.2. Different sizes and patterns of the local substructure

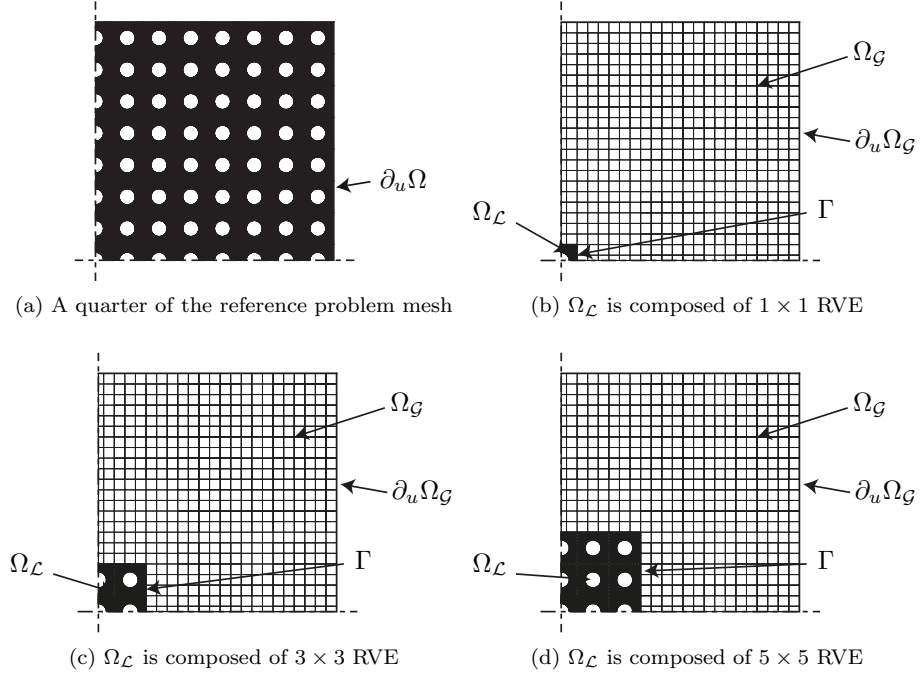


Figure 12: Illustration of a quarter mesh of the reference and the coupled problems for different sizes of the local substructure.

Let us consider the coupled problems with the meshes of **Figures 12b-12d**. The central parts $\Omega_{\mathcal{L}}$ are respectively composed by a set of 1 RVE, 3 \times 3 RVEs and 5 \times 5 RVEs. The RVE have the same dimensions and material parameters as in the previous sections. That is to say l , the size of one RVE, is taken to be of 2 mm. The material parameters are the ones given in **Section 5.1** for the common steel material. The external part $\Omega_{\mathcal{G}}$ is larger than in the previous sections: 30 mm. As previously, this one is modeled by a homogenized behavior with the parameters also given in **Section 5.1**.

The reference mesh for the full microscopic description is shown in **Figure 12a**. It is composed by a set of 15 \times 15 RVEs and the material parameters are the same as in $\Omega_{\mathcal{L}}$.

As previously, the boundary conditions on $\partial_u \Omega_{\mathcal{G}}$ satisfy equation (23) with the same components of the deformation gradient tensor as in the example 2.

The solutions given by the reference problem and by the coupled problem are compared through the error defined by (1). The local error maps are shown in **Figure 13** and their maximum and mean values are displayed in the **Table 1**.

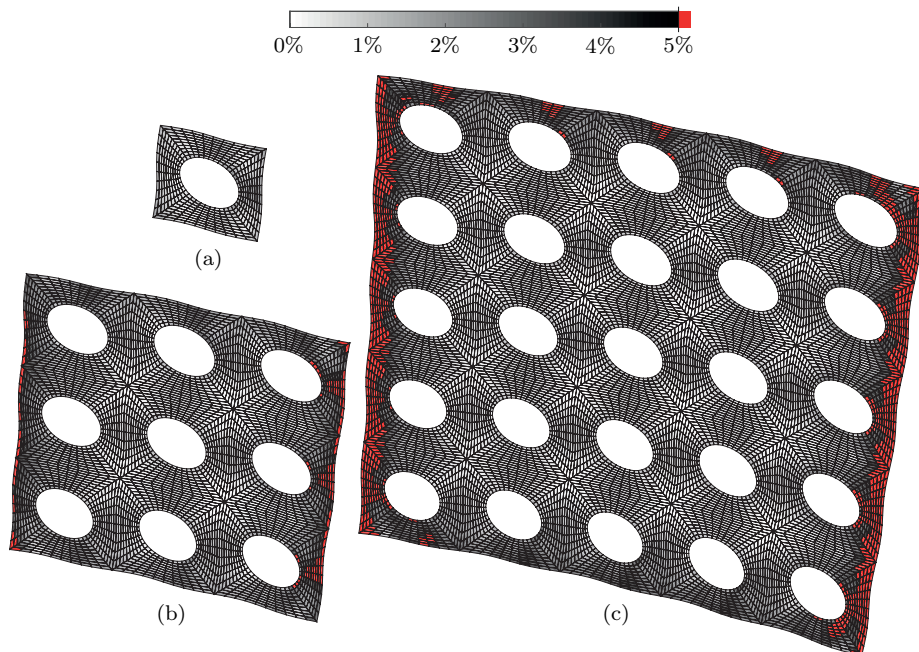


Figure 13: Error maps based on the energetic criterion e_E defined on (1) between \underline{u} the displacement solution of the coupled problem on $\Omega_{\mathcal{L}}$ and $\underline{u}_{\text{ref}}$ the displacement solution of the corresponding part of the reference problem. $\Omega_{\mathcal{L}}$ is respectively composed by a single RVE (a) a set of 3×3 RVEs (b) and a set of 5×5 RVEs (c). The colorscale is truncated after 5%.

	1 \times 1 RVE	3 \times 3 RVEs	5 \times 5 RVEs
e_E^{\max}	3%	7.7%	12%
e_E^{mean}	1.1%	1.7%	1.9%

Table 1: Maximum energy local error for different scenarios of local substructures.

As shown in **Figure 13**, the maximum local error increases with the number of RVEs in $\Omega_{\mathcal{L}}$ because the local substructure is getting closer to the boundary $\partial_u \Omega_{\mathcal{G}}$. Indeed, the coupled solutions used to compute the error maps in **Figure 13** are obtained for local structures of increasing sizes. But, the reference domain is fixed thus the corresponding local regions are getting closer to the outer edges. Similar tendency is observed for a single RVE according to its proximity to the outer edges. Comparing the solutions obtained for the same local structure but different sizes of global and reference domains, the error decreases from a mean value of 2.6% (**Figure 10** - exemple 2, column 3) to a mean value of 1.1% (**Figure 13a**), when the local region is far from the outer edge.

The error is due to edge effects as explained in the **Remark 3** because the reference solution tends to be periodic for the most centrally located cells but the applied boundary conditions are not compatible with the periodicity

assumptions being used. Thus, the error increases as the zoom gets closer to the outer edges. However, it remains low and localized on the boundaries of $\Omega_{\mathcal{L}}$ which satisfy the Saint-Venant principle as the macroscopic quantities are well transmitted between the local and global substructures. The error comes from the microscopic fields and does not penetrate into the interior of $\Omega_{\mathcal{L}}$.

As a result, periodicity conditions (20) are relevant in ideal cases from a homogenization point of view. In other cases, for example non-periodic situations, they could be advantageously modified according to the case treated.

6. Conclusions

In this paper, a global-local interface coupling technique has been proposed in order to couple a heterogeneous microscopic (local) model with a first-order homogenized (global) model. The coupling technique is based on a second-order homogenization strategy and deals with non-uniform loadings at the RVE scale. It is associated with a scale separation of interface quantities on the coupling interface which makes the formulation independent of the meshes considered.

The proposed coupling technique has been validated on different examples appropriate for homogenization assumptions and for different loading cases. It gives excellent results in comparison with the considered Mortar interface coupling technique for compatible models and was shown to be nearly insensible to mesh discretizations. In more general cases, the coupling and periodicity conditions could be advantageously modified according to the case.

The proposed coupling conditions are given for a local model fully shrouded in the global model. The current work is to extend this technique and formulate coupling conditions for different localizations of the local model, including cases near the domain boundaries. Moreover, a non-intrusive version of the approach is currently being developed.

Acknowledgements

This work was supported by the French *National Association for Research and Technology* (ANRT) through the research grant CIFRE 2016/0517.

Appendix A. Two-scale separation of dual interface quantities according to a given scalar product

Appendix A.1. Separation of a force distribution into a macroscopic and microscopic parts

Let us consider an interface displacement field $\underline{W}_\gamma \in \mathcal{W}_\gamma$ defined on γ . The macroscopic part of this displacement field, \underline{W}_γ^M , is defined as the projection onto a subspace \mathcal{W}_γ^M of \mathcal{W}_γ with a finite dimension $n_M = \dim(\mathcal{W}_\gamma^M)$. Thus, the following projector can be introduced:

$$\begin{aligned} \mathbf{\Pi}_\gamma^{M,W} : \mathcal{W}_\gamma &\rightarrow \mathcal{W}_\gamma^M \\ \underline{W}_\gamma &\mapsto \mathbf{\Pi}_\gamma^{M,W}(\underline{W}_\gamma) = \underline{W}_\gamma^M \end{aligned}$$

The microscopic part, \underline{W}_γ^m , of \underline{W}_γ belongs to the complementary subspace \mathcal{W}_γ^m of $\mathcal{W}_\gamma = \mathcal{W}_\gamma^M \oplus \mathcal{W}_\gamma^m$ as follows:

$$\underline{W}_\gamma^m = \underline{W}_\gamma - \underline{W}_\gamma^M = (I_d - \mathbf{\Pi}_\gamma^{M,W})(\underline{W}_\gamma)$$

Consequently, one has $\underline{W}_\gamma = \underline{W}_\gamma^M + \underline{W}_\gamma^m$. Let us introduce the following work bilinear form on $\mathcal{W}_\gamma \times \mathcal{F}_\gamma$:

$$\begin{aligned} (\cdot, \cdot)_\gamma : \mathcal{W}_\gamma \times \mathcal{F}_\gamma &\rightarrow \mathbb{R} \\ (\underline{W}_\gamma, \underline{F}_\gamma)_\gamma &\mapsto \int_\gamma \underline{W}_\gamma \cdot \underline{F}_\gamma \, d\Gamma \end{aligned}$$

The microscopic part \underline{F}_γ^m and the macroscopic part \underline{F}_γ^M of force distribution $\underline{F}_\gamma (= \underline{F}_\gamma^M + \underline{F}_\gamma^m)$ are defined such that the work is uncoupled between scales:

$$(\underline{W}_\gamma, \underline{F}_\gamma)_\gamma = (\underline{W}_\gamma^M, \underline{F}_\gamma^M)_\gamma + (\underline{W}_\gamma^m, \underline{F}_\gamma^m)_\gamma$$

Consequently, the macroscopic force $\underline{F}_\gamma^M \in \mathcal{F}_\gamma^M$ is defined by:

$$\forall \underline{W}_\gamma^{M*} \in \mathcal{W}_\gamma^M, (\underline{W}_\gamma^{M*}, \underline{F}_\gamma) = (\underline{W}_\gamma^{M*}, \underline{F}_\gamma^M) \quad (\text{A.1})$$

The spaces \mathcal{W}_γ^M and \mathcal{F}_γ^M have therefore the same dimension : n_M .

Appendix A.2. Macroscopic projector definition

Let us introduce \mathbf{e}_γ^M , a basis of the subspace $\mathcal{W}_\gamma^M \subset \mathcal{F}_\gamma \cap \mathcal{W}_\gamma$: $\mathbf{e}_\gamma^M = (\{\underline{e}_k^M\}_{k=1..n_M})$. Then, the bilinear form $(\cdot, \cdot)_\gamma$ is a scalar product on the subspace generated by the basis \mathbf{e}_γ^M and:

$$\mathbf{\Pi}_\gamma^{M,W}(\underline{W}_\gamma) = \underline{W}_\gamma^M = \sum_{k=1}^{n_M} (\underline{W}_\gamma, \underline{e}_k^M)_\gamma \underline{e}_k^M = \sum_{k=1}^{n_M} [\underline{W}_\gamma^M]_k \underline{e}_k^M = \mathbf{e}_\gamma^M [\underline{W}_\gamma^M]_{\mathbf{e}_\gamma^M}$$

where the k -th component of \underline{W}_γ^M in \underline{e}_k^M is in this case $[\underline{W}_\gamma^M]_k = (\underline{W}_\gamma, \underline{e}_k^M)_\gamma$. The vector of the n_M macro-displacement components in the macro-basis \mathbf{e}_γ^M is denoted by $[\underline{W}_\gamma^M]_{\mathbf{e}_\gamma^M}$. Moreover, since \mathbf{e}_γ^M is also a basis of \mathcal{F}_γ^M , one also has:

$$\mathbf{\Pi}_\gamma^{M,F}(\underline{F}_\gamma) = \underline{F}_\gamma^M = \sum_{k=1}^{n_M} (\underline{F}_\gamma, \underline{e}_k^M)_\gamma \underline{e}_k^M$$

and :

$$(\underline{W}_\gamma^M, \underline{F}_\gamma^M)_\gamma = \sum_{k=1}^{n_M} \sum_{j=1}^{n_M} [\underline{W}_\gamma^M]_k (\underline{e}_k^M, \underline{e}_j^M)_\gamma [\underline{F}_\gamma^M]_j$$

If the basis \mathbf{e}_γ^M is orthonormal in the sense of scalar product $(\cdot, \cdot)_\gamma$ on the subspace generated by the basis \mathbf{e}_γ^M , the macrowork is then defined by:

$$(\underline{W}_\gamma^M, \underline{F}_\gamma^M)_\gamma = [\underline{W}_\gamma^M]_{\mathbf{e}_\gamma^M}^T [\underline{F}_\gamma^M]_{\mathbf{e}_\gamma^M}$$

and, finally the macroscopic projector for displacement, $\mathbf{\Pi}_\gamma^{M,W}$, is similar to the macroscopic projector for force distribution: $\mathbf{\Pi}_\gamma^{M,W} = \mathbf{\Pi}_\gamma^{M,F} = \mathbf{\Pi}_\gamma^M$. Then :

$$\mathbf{\Pi}_\gamma^M(\underline{W}_\gamma) = \underline{W}_\gamma^M = \sum_{k=1}^{n_M} [\underline{W}_\gamma^M]_k \underline{e}_k^M = \sum_{k=1}^{n_M} (\underline{W}_\gamma, \underline{e}_k^M)_\gamma \underline{e}_k^M \quad (\text{A.2})$$

and:

$$\mathbf{\Pi}_\gamma^M(\underline{F}_\gamma) = \underline{F}_\gamma^M = \sum_{k=1}^{n_M} [\underline{F}_\gamma^M]_k \underline{e}_k^M = \sum_{k=1}^{n_M} (\underline{F}_\gamma, \underline{e}_k^M)_\gamma \underline{e}_k^M \quad (\text{A.3})$$

For further details, interested reader can refer to [32].

Appendix B. Homogenized Macroscopic Quantities

For the particular case of a two-dimensional rectangular RVE presented in **Figure B.14**, the 12 homogenization macroscopic quantities, ε_{xx}^M , ε_{yy}^M , ε_{xy}^M , G_{xxx}^M , G_{yyy}^M , G_{xyy}^M , G_{yxx}^M , G_{xxy}^M , G_{xyx}^M , G_{yyx}^M , G_{yxy}^M , G_{yxx}^M , as well as the RVE rigid body motion components u_y^C , u_x^C and ω^M can be determined by the 12 relations imposed on \underline{W} by (10)-(12). The relations between the interface macro-components and the homogenization macroscopic quantities are given below according to the following notations:

$$\begin{aligned} \left\langle [\underline{W}^M]_{e_2^M} \right\rangle_{nr/ml} &= n[\underline{W}_r^M]_{e_2^M} + m[\underline{W}_l^M]_{e_2^M} \\ \left[[\underline{W}^M]_{e_4^M} \right]_{nt/md} &= n[\underline{W}_t^M]_{e_4^M} - m[\underline{W}_d^M]_{e_4^M} \end{aligned}$$

The RVE rotation and strain components are given only by mean parts of interface displacements ($[\underline{W}^M]_{e_1^M}$ and $[\underline{W}^M]_{e_2^M}$):

$$\begin{aligned} \omega^M &= -\frac{1}{2L_x L_y} \left[\sqrt{L_x} \left\langle [\underline{W}^M]_{e_1^M} \right\rangle_{1t/1d} + \sqrt{L_y} \left\langle [\underline{W}^M]_{e_1^M} \right\rangle_{1r/1l} \right] \\ \varepsilon_{xx}^M &= \frac{1}{L_x \sqrt{L_y}} \left\langle [\underline{W}^M]_{e_2^M} \right\rangle_{1r/1l} \\ \varepsilon_{yy}^M &= \frac{1}{\sqrt{L_x} L_y} \left\langle [\underline{W}^M]_{e_2^M} \right\rangle_{1t/1d} \\ \varepsilon_{xy}^M &= \frac{1}{2L_x L_y} \left[\sqrt{L_x} \left\langle [\underline{W}^M]_{e_1^M} \right\rangle_{1t/1d} - \sqrt{L_y} \left\langle [\underline{W}^M]_{e_1^M} \right\rangle_{1r/1l} \right] \end{aligned}$$

The two components of \mathbf{G}_M that are expressed only in terms of linear components (rotation $[\underline{W}^M]_{e_3^M}$ and extension $[\underline{W}^M]_{e_4^M}$) are written as:

$$\begin{aligned} G_{xyx}^M &= \frac{1}{L_y} \sqrt{\frac{12}{L_x^3}} \left[[\underline{W}^M]_{e_4^M} \right]_{1t/1d} \left(= G_{xxy}^M = -\frac{1}{L_x} \sqrt{\frac{12}{L_y^3}} \left[[\underline{W}^M]_{e_3^M} \right]_{1r/1l} \right) \\ G_{yyx}^M &= \frac{1}{L_x} \sqrt{\frac{12}{L_y^3}} \left[[\underline{W}^M]_{e_4^M} \right]_{1r/1l} \left(= G_{yxy}^M = \frac{1}{L_y} \sqrt{\frac{12}{L_x^3}} \left[[\underline{W}^M]_{e_3^M} \right]_{1t/1d} \right) \end{aligned}$$

The other components of \mathbf{G}_M are written as a function of the macroscopic interface displacements and the displacement in a corner A with $u_x^A = \underline{u}(A) \cdot \underline{e}_x$, $u_y^A = \underline{u}(A) \cdot \underline{e}_y$:

$$\begin{aligned} G_{xxx}^M &= \frac{6}{L_x^2 \sqrt{L_y}} \left[\left\langle [\underline{W}^M]_{e_2^M} \right\rangle_{1r/1l} + \sqrt{3} \left[[\underline{W}^M]_{e_3^M} \right]_{1r/1l} + \right. \\ &\quad \left. + 2\sqrt{\frac{L_y}{L_x}} [\underline{W}_d^M]_{e_1^M} + 2\sqrt{L_y} u_x^A \right] \end{aligned}$$

$$\begin{aligned}
G_{yyy}^M &= \frac{6}{L_y^2 \sqrt{L_x}} \left[\langle [W^M]_{e_2^M} \rangle_{1t/1d} - \sqrt{3} [W^M]_{e_3^M} \Big|_{1t/1d} - \right. \\
&\quad \left. - 2 \sqrt{\frac{L_x}{L_y}} [W^M]_{e_1^M} + 2 \sqrt{L_x} u_y^A \right] \\
G_{xyy}^M &= \frac{6}{\sqrt{L_x} L_y^2} \left[\langle [W^M]_{e_1^M} \rangle_{1t/1d} + \sqrt{\frac{3L_x}{L_y}} [W^M]_{e_3^M} \Big|_{1r/1l} + \right. \\
&\quad \left. + 2 \sqrt{L_x} \left(\frac{1}{\sqrt{L_y}} [W^M]_{e_2^M} + u_x^A \right) \right] \\
G_{yxx}^M &= -\frac{6}{\sqrt{L_y} L_x^2} \left[\langle [W^M]_{e_1^M} \rangle_{1r/1l} + \sqrt{\frac{3L_y}{L_x}} [W^M]_{e_3^M} \Big|_{1t/1d} - \right. \\
&\quad \left. - 2 \sqrt{L_y} \left(\frac{1}{\sqrt{L_x}} [W^M]_{e_2^M} + u_y^A \right) \right]
\end{aligned}$$

The RVE rigid body translation components are given by:

$$\begin{aligned}
u_x^C &= -\frac{1}{4\sqrt{L_y}} \left[4\sqrt{3} [W^M]_{e_3^M} \Big|_{1r/1l} + \langle [W^M]_{e_2^M} \rangle_{1r/7l} + \right. \\
&\quad \left. + \sqrt{\frac{L_y}{L_x}} \langle [W^M]_{e_1^M} \rangle_{1t/7d} + 8\sqrt{L_y} u_x^A \right] \\
u_y^C &= \frac{1}{4\sqrt{L_x}} \left[4\sqrt{3} [W^M]_{e_3^M} \Big|_{1t/1d} - \langle [W^M]_{e_2^M} \rangle_{1t/7d} + \right. \\
&\quad \left. + \sqrt{\frac{L_x}{L_y}} \langle [W^M]_{e_1^M} \rangle_{1r/7l} - 8\sqrt{L_x} u_y^A \right]
\end{aligned}$$

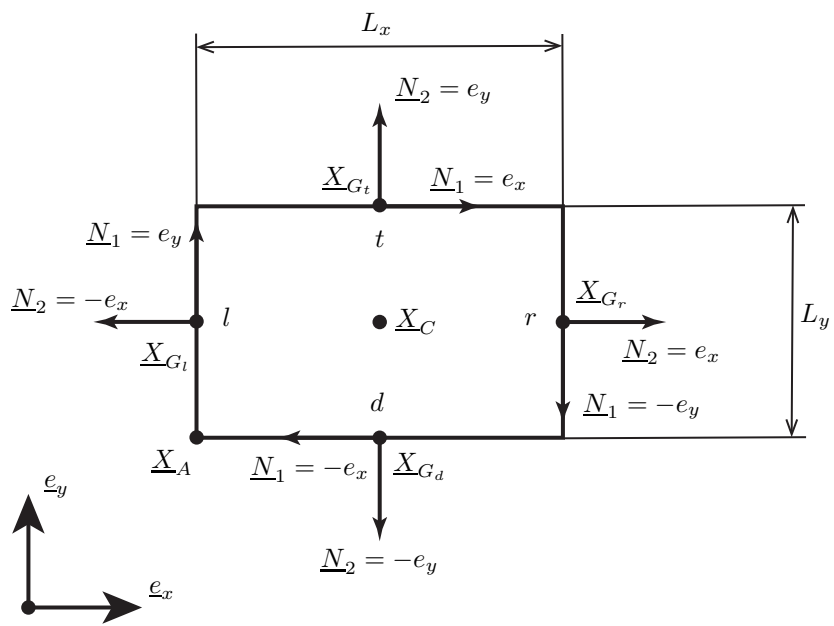


Figure B.14: Rectangular two-dimensional RVE with interface notations

Appendix C. Discretization and solution strategy

Appendix C.1. Discretization

Let us introduce the finite element approximation spaces $\mathcal{U}_s^h \subset \mathcal{U}_s$, $\mathcal{F}_s^h \subset \mathcal{F}_s$ and $\mathcal{W}_s^h \subset \mathcal{W}_s$ such that the displacement on the substructure $s \in \{\mathcal{G}, \mathcal{L}\}$ is written as:

$$\underline{u}_s^h(\underline{x}) = \sum_{k=1}^{N_s} [U_s]_k \underline{\varphi}_k(\underline{x})$$

the displacement on the interface Γ is written as:

$$\underline{W}_s^h(\underline{x}) = \sum_{k=1}^{N_\Gamma} [W_s]_k \underline{\psi}_k(\underline{x})$$

and the k -th discretized vector of macroscopic basis function is written as:

$$\underline{e}_k^{M,h}(\underline{x}) = \sum_{j=1}^{N_\Gamma} [e_k^M]_j \underline{\psi}_j(\underline{x})$$

Approximation spaces for the interface quantities and the displacement quantities has to be carefully chosen so that the inf-sup conditions (or LBB-conditions) are satisfied [2, 5, 9, 10]. In the following, one considers that $\mathcal{W}_s^h = \mathcal{F}_s^h$. For the sake of generality, the interface shape functions ψ are not necessary the restriction of internal shape functions $\varphi|_\gamma$. Thus, the kinematic admissibility between $\underline{u}_{s|\gamma}$ and \underline{W}_s can be classically discretized as follows:

$$[\mathbf{N}_{s_\gamma}][\mathbf{B}_{s_\gamma}][U_s] = [\mathbf{M}_{s_\gamma}][W_s]$$

where $[\mathbf{B}_{s_\gamma}]$ is a boolean operator (discretized trace operator) that restricts the nodal vector of unknowns $[U_s]$ to the interface γ . The matrices $[\mathbf{N}_{s_\gamma}]$ and $[\mathbf{M}_{s_\gamma}]$ are defined by:

$$[\mathbf{N}_{s_\gamma}]_{ij} = \left(\underline{\psi}_i, \underline{\varphi}_{j|\Gamma} \right)_\gamma \quad (\text{C.1})$$

$$[\mathbf{M}_{s_\gamma}]_{ij} = \left(\underline{\psi}_i, \underline{\psi}_j \right)_\gamma \quad (\text{C.2})$$

Since the matrix $[\mathbf{M}_{s_\gamma}]$ is similar to a mass matrix, it is invertible and:

$$[W_{s_\gamma}] = \underbrace{[\mathbf{M}_{s_\gamma}]^{-1}[\mathbf{N}_{s_\gamma}][\mathbf{B}_{s_\gamma}]}_{[\mathbf{B}_{s_\gamma}]}[U_s] \quad (\text{C.3})$$

By introducing $[e_\Gamma^M] = [[e_1^M], [e_2^M], \dots, [e_{n_M}^M]]$ the $n_\Gamma \times n_M$ discretized macro-basis where column l corresponds to the discretized macro-basis function l , $[e_l^M]$, one can show that the macroscopic projectors Π_γ^M can be discretized as follows:

$$[\mathbf{\Pi}_{s_\gamma}^M] = [e_{s_\gamma}^M]^t [e_{s_\gamma}^M] [\mathbf{M}_{s_\gamma}]$$

Thus, one deduces that the discretized macroscopic and microscopic displacements are such that:

$$\begin{cases} [W_{s_\gamma}^m] &= \left([\mathbf{I}_d] - [\mathbf{\Pi}_{s_\gamma}^M] \right) [\overline{\mathbf{B}}_{s_\gamma}] [U_s] \\ [W_{s_\gamma}^M] &= [\mathbf{e}_{s_\gamma}^M] [W_{s_\gamma}^M]_{e^M} = [\mathbf{\Pi}_{s_\gamma}^M] [\overline{\mathbf{B}}_{s_\gamma}] [U_s] \end{cases} \quad (\text{C.4})$$

where $[W_{s_\gamma}^M]_{e^M}$ is a n_M -length vector of components of $\underline{W}_{s_\gamma}^M$ in the discretized macro-basis $[\mathbf{e}_{s_\gamma}^M]$. Similar approximations can be given for an interface force \underline{F}_{s_γ} . Due to the orthogonality of the macro-basis function, one has the following property:

$${}^t[\mathbf{e}_{s_\gamma}^M] [\mathbf{M}_{s_\gamma}] [\mathbf{e}_{s_\gamma}^M] = [\mathbf{I}_d] \quad (\text{C.5})$$

Appendix C.2. Discretized saddle-point problem

The substitution of discretized quantities into the weak formulation gives the following monolithic finite element linear system:

$$\begin{bmatrix} [\mathbf{K}] & [\mathbf{C}]^T & [\mathbf{P}]^T \\ [\mathbf{C}] & [\mathbf{0}] & [\mathbf{0}] \\ [\mathbf{P}] & [\mathbf{0}] & [\epsilon] \end{bmatrix} \begin{bmatrix} [U] \\ [\Lambda_C] \\ [\Lambda_P] \end{bmatrix} = \begin{bmatrix} [F] \\ [0] \\ [0] \end{bmatrix} \quad (\text{C.6})$$

where:

$$\begin{aligned} [\mathbf{K}] &= \begin{bmatrix} [\mathbf{K}_G] & [\mathbf{0}] \\ [\mathbf{0}] & [\mathbf{K}_L] \end{bmatrix} \\ [U] &= \begin{bmatrix} [U_G] \\ [U_L] \end{bmatrix} \\ [F] &= \begin{bmatrix} [F_G] \\ [F_L] \end{bmatrix} \end{aligned}$$

with $[\mathbf{K}_G]$ and $[\mathbf{K}_L]$ the stiffness matrices of the global and the local substructures respectively, $[U_G]$ and $[U_L]$ the nodal vector of unknowns of the global and the local substructures, $[F_G]$, $[F_L]$ the generalized forces applied over the global and the local substructures and $[\Lambda_C]$, $[\Lambda_P]$ the discretized Lagrangian multipliers associated to relations (10)-(14).

The discretized coupling operator $[\mathbf{C}]$ in (C.6) is defined by:

$$[\mathbf{C}] = \begin{bmatrix} [\mathbf{C}_G^U] & -[\mathbf{C}_L^U] \\ [\mathbf{P}_G^L] & -[\mathbf{P}_L^L] \\ [\mathbf{B}_{G_A}] & -[\mathbf{B}_{L_A}] \end{bmatrix}$$

where the coupling operators on the substructure $s \in \{\mathcal{L}, \mathcal{G}\}$ concerning the macro-basis components $p \in \{T, L, Q\}$ are defined by:

$$[\mathbf{C}_s^p] = \begin{bmatrix} {}^t[\mathbf{e}_{s_d}^p] [\mathbf{M}_{s_d}] [\overline{\mathbf{B}}_{s_d}] \\ {}^t[\mathbf{e}_{s_r}^p] [\mathbf{M}_{s_r}] [\overline{\mathbf{B}}_{s_r}] \\ {}^t[\mathbf{e}_{s_t}^p] [\mathbf{M}_{s_t}] [\overline{\mathbf{B}}_{s_t}] \\ {}^t[\mathbf{e}_{s_l}^p] [\mathbf{M}_{s_l}] [\overline{\mathbf{B}}_{s_l}] \end{bmatrix}$$

and the periodicity operators of linear macrocomponent on the substructure s by:

$$[\mathbf{P}_s^L] = \begin{bmatrix} {}^t[e_{s_t}^L][\mathbf{M}_{s_t}][\overline{\mathbf{B}}_{s_t}] - {}^t[e_{s_d}^L][\mathbf{M}_{s_d}][\overline{\mathbf{B}}_{s_d}] \\ {}^t[e_{s_r}^L][\mathbf{M}_{s_r}][\overline{\mathbf{B}}_{s_r}] - {}^t[e_{s_l}^L][\mathbf{M}_{s_l}][\overline{\mathbf{B}}_{s_l}] \end{bmatrix}$$

The discretized trace operator $[\mathbf{B}_{s_A}]$, on the substructure s , restricts the nodal vector of unknowns $[U_s]$ to the A corner.

The discretized periodicity operator $[\mathbf{P}]$ in (C.6) is defined by:

$$[\mathbf{P}] = \begin{bmatrix} [\mathbf{P}_{\mathcal{G}}^Q] & [\mathbf{0}] \\ [\mathbf{P}_{\mathcal{G}}^m] & [\mathbf{0}] \\ [\mathbf{0}] & [\mathbf{P}_{\mathcal{L}}^Q] \\ [\mathbf{0}] & [\mathbf{P}_{\mathcal{L}}^m] \end{bmatrix}$$

where the periodicity operators of quadratic macrocomponent on substructure $s \in \{\mathcal{L}, \mathcal{G}\}$ is defined by:

$$[\mathbf{P}_s^Q] = \begin{bmatrix} {}^t[e_{s_t}^Q][\mathbf{M}_{s_t}][\overline{\mathbf{B}}_{s_t}] - {}^t[e_{s_d}^Q][\mathbf{M}_{s_d}][\overline{\mathbf{B}}_{s_d}] \\ {}^t[e_{s_r}^Q][\mathbf{M}_{s_r}][\overline{\mathbf{B}}_{s_r}] - {}^t[e_{s_l}^Q][\mathbf{M}_{s_l}][\overline{\mathbf{B}}_{s_l}] \end{bmatrix}$$

and the periodicity operator of the micro-components on local substructure, with a periodic mesh, is given by:

$$[\mathbf{P}_{\mathcal{L}}^m] = \begin{bmatrix} [\mathbf{M}_{\mathcal{L}_t}]([\mathbf{I}_d] - [\mathbf{\Pi}_{\mathcal{L}_t}])[\overline{\mathbf{B}}_{\mathcal{L}_t}] - [\mathbf{M}_{\mathcal{L}_d}]([\mathbf{I}_d] - [\mathbf{\Pi}_{\mathcal{L}_d}])[\overline{\mathbf{B}}_{\mathcal{L}_d}] \\ [\mathbf{M}_{\mathcal{L}_r}]([\mathbf{I}_d] - [\mathbf{\Pi}_{\mathcal{L}_r}])[\overline{\mathbf{B}}_{\mathcal{L}_r}] - [\mathbf{M}_{\mathcal{L}_l}]([\mathbf{I}_d] - [\mathbf{\Pi}_{\mathcal{L}_l}])[\overline{\mathbf{B}}_{\mathcal{L}_l}] \end{bmatrix}$$

The penalty term $[\epsilon]$, is added to system (C.6) in order to enforce periodicity of microscopic displacements and is defined by:

$$[\epsilon] = \begin{bmatrix} [\mathbf{0}] & [\mathbf{0}] & [\mathbf{0}] & [\mathbf{0}] \\ [\mathbf{0}] & -\varepsilon[\mathbf{M}_{\mathcal{G}}^P] & [\mathbf{0}] & [\mathbf{0}] \\ [\mathbf{0}] & [\mathbf{0}] & [\mathbf{0}] & [\mathbf{0}] \\ [\mathbf{0}] & [\mathbf{0}] & [\mathbf{0}] & -\varepsilon[\mathbf{M}_{\mathcal{L}}^P] \end{bmatrix}$$

where $\varepsilon > 0$ and as the meshes of the global and the local substructures are assumed to be periodic:

$$[\mathbf{M}_s^P] = \begin{bmatrix} [\mathbf{M}_{s_d}] & [\mathbf{0}] \\ [\mathbf{0}] & [\mathbf{M}_{s_t}] \end{bmatrix} = \begin{bmatrix} [\mathbf{M}_{s_t}] & [\mathbf{0}] \\ [\mathbf{0}] & [\mathbf{M}_{s_r}] \end{bmatrix}$$

One can refer to [5] (sections 3.2.2 and 3.2.3) for further details on the penalty term $[\epsilon]$.

References

- [1] Annavarapu, C., Hautefeuille, M., Dolbow, J. E., 2012. A robust Nitsche's formulation for interface problems. *Computer Methods in Applied Mechanics and Engineering* 225-228, 44–54.
- [2] Babuška, I., 1973. The finite element method with Lagrangian multipliers. *Numerische Mathematik* 20 (3), 179–192.
- [3] Belgacem, F. B., 1999. The Mortar finite element method with Lagrange multipliers. *Numerische Mathematik* 84 (2), 173–197.
- [4] Bernardi, C., Maday, Y., Rapetti, F., 2005. Basics and some applications of the mortar element method. *GAMM-Mitteilungen* 28 (2), 97–123.
- [5] Boffi, D., Brezzi, F., Fortin, M., 2013. *Mixed Finite Element Methods and Applications*. Vol. 44 of Springer Series in Computational Mathematics. Springer, Berlin Heidelberg.
- [6] Bosco, E., Kouznetsova, V. G., Coenen, E. W. C., Geers, M. G. D., Salvadori, A., 2014. A multiscale framework for localizing microstructures towards the onset of macroscopic discontinuity. *Computational Mechanics* 54 (2), 299–319.
- [7] Bouclier, R., Passieux, J.-C., 2018. A Nitsche-based non-intrusive coupling strategy for global/local isogeometric structural analysis. *Computer Methods in Applied Mechanics and Engineering* 340, 253–277.
- [8] Bouclier, R., Passieux, J.-C., Salaün, M., 2017. Development of a new, more regular, mortar method for the coupling of NURBS subdomains within a NURBS patch: Application to a non-intrusive local enrichment of NURBS patches. *Computer Methods in Applied Mechanics and Engineering* 316, 123–150.
- [9] Brezzi, F., 1974. On the existence, uniqueness and approximation of saddle-point problems arising from lagrangian multipliers. *ESAIM: Mathematical Modelling and Numerical Analysis - Modélisation Mathématique et Analyse Numérique* 8 (R2), 129–151.
- [10] Brezzi, F., Fortin, M., 1991. Approximation of Saddle Point Problems. In: *Mixed and Hybrid Finite Element Methods*. Springer, pp. 36–88.
- [11] Brivadis, E., Buffa, A., Wohlmuth, B., Wunderlich, L., 2015. Isogeometric mortar methods. *Computer Methods in Applied Mechanics and Engineering* 284, 292–319.
- [12] Coenen, E. W. C., Kouznetsova, V. G., Geers, M. G. D., 2010. Computational homogenization for heterogeneous thin sheets. *International Journal for Numerical Methods in Engineering* 83 (8-9), 1180–1205.

- [13] Dolbow, J., Harari, I., 2008. An efficient finite element method for embedded interface problems. *International Journal for Numerical Methods in Engineering* 78 (2), 229–252.
- [14] Dornisch, W., Vitucci, G., Klinkel, S., 2015. The weak substitution method – an application of the mortar method for patch coupling in NURBS-based isogeometric analysis. *International Journal for Numerical Methods in Engineering* 103 (3), 205–234.
- [15] Duval, M., Passieux, J.-C., Salaün, M., Guinard, S., 2016. Non-intrusive Coupling: Recent Advances and Scalable Nonlinear Domain Decomposition. *Archives of Computational Methods in Engineering* 23 (1), 17–38.
- [16] Feyel, F., 2003. A multilevel finite element method (FE2) to describe the response of highly non-linear structures using generalized continua. *Computer Methods in Applied Mechanics and Engineering* 192 (28), 3233–3244.
- [17] Feyel, F., Chaboche, J.-L., 2000. FE2 multiscale approach for modelling the elastoviscoplastic behaviour of long fibre SiC/Ti composite materials. *Computer Methods in Applied Mechanics and Engineering* 183 (3), 309–330.
- [18] Forest, S., 1998. Mechanics of generalized continua: Construction by homogenization. *Le Journal de Physique IV* 08 (PR4), Pr4–39–Pr4–48.
- [19] Gendre, L., Allix, O., Gosselet, P., Comte, F., 2009. Non-intrusive and exact global/local techniques for structural problems with local plasticity. *Computational Mechanics* 44 (2), 233–245.
- [20] Guguin, G., Allix, O., Gosselet, P., Guinard, S., 2014. Nonintrusive coupling of 3D and 2D laminated composite models based on finite element 3D recovery. *International Journal for Numerical Methods in Engineering* 98 (5), 324–343.
- [21] Guguin, G., Allix, O., Gosselet, P., Guinard, S., 2016. On the computation of plate assemblies using realistic 3D joint model: A non-intrusive approach. *Advanced Modeling and Simulation in Engineering Sciences* 3 (1), 16.
- [22] Guidault, P.-A., Allix, O., Champaney, L., Cornuault, C., 2008. A multiscale extended finite element method for crack propagation. *Computer Methods in Applied Mechanics and Engineering* 197 (5), 381–399.
- [23] Guinard, S., Bouclier, R., Tonioli, M., Passieux, J.-C., 2018. Multiscale analysis of complex aeronautical structures using robust non-intrusive coupling. *Advanced Modeling and Simulation in Engineering Sciences* 5 (1), 1.
- [24] Kaczmarczyk, Ł., Pearce, C. J., Bićanić, N., 2008. Scale transition and enforcement of RVE boundary conditions in second-order computational homogenization. *International Journal for Numerical Methods in Engineering* 74 (3), 506–522.

- [25] Kanit, T., Forest, S., Galliet, I., Mounoury, V., Jeulin, D., 2003. Determination of the size of the representative volume element for random composites: Statistical and numerical approach. *International Journal of Solids and Structures* 40 (13), 3647–3679.
- [26] Kouznetsova, V., Brekelmans, W. a. M., Baaijens, F. P. T., 2001. An approach to micro-macro modeling of heterogeneous materials. *Computational Mechanics* 27 (1), 37–48.
- [27] Kouznetsova, V. G., Geers, M. G. D., Brekelmans, W. a. M., 2002. Multi-scale constitutive modelling of heterogeneous materials with a gradient-enhanced computational homogenization scheme. *International Journal for Numerical Methods in Engineering* 54 (8), 1235–1260.
- [28] Kouznetsova, V. G., Geers, M. G. D., Brekelmans, W. A. M., 2004. Multi-scale second-order computational homogenization of multi-phase materials: A nested finite element solution strategy. *Computer Methods in Applied Mechanics and Engineering* 193 (48), 5525–5550.
- [29] Kouznetsova, V. G., Geers, M. G. D., Brekelmans, W. a. M., 2004. Size of a Representative Volume Element in a Second-Order Computational Homogenization Framework. *International Journal for Multiscale Computational Engineering* 2 (4).
- [30] Kouznetsova, Varvara, 2002. Computational homogenization for the multi-scale analysis of multi-phase materials. Ph.D. thesis, Technische Universiteit Eindhoven.
- [31] Lacour, C., Maday, Y., 1997. Two different approaches for matching non-conforming grids: The Mortar Element method and the Feti Method. *BIT Numerical Mathematics* 37 (3), 720–738.
- [32] Ladevèze, P., Loiseau, O., Dureisseix, D., 2001. A micro-macro and parallel computational strategy for highly heterogeneous structures. *International Journal for Numerical Methods in Engineering* 52 (1-2), 121–138.
- [33] Ladevèze, P., Nouy, A., Loiseau, O., 2002. A multiscale computational approach for contact problems. *Computer Methods in Applied Mechanics and Engineering* 191 (43), 4869–4891.
- [34] Miehe, C., Schröder, J., Schotte, J., 1999. Computational homogenization analysis in finite plasticity Simulation of texture development in polycrystalline materials. *Computer Methods in Applied Mechanics and Engineering* 171 (3), 387–418.
- [35] Nguyen, V. P., Kerfriden, P., Brino, M., Bordas, S. P. A., Bonisoli, E., 2014. Nitsche’s method for two and three dimensional NURBS patch coupling. *Computational Mechanics* 53 (6), 1163–1182.

- [36] Oden, J. T., Zohdi, T. I., 1997. Analysis and adaptive modeling of highly heterogeneous elastic structures. *Computer Methods in Applied Mechanics and Engineering* 148 (3), 367–391.
- [37] Ostoja-Starzewski, M., Boccarda, S. D., Jasiuk, I., 1999. Couple-stress moduli and characteristic length of a two-phase composite. *Mechanics Research Communications* 26 (4), 387–396.
- [38] Otero, F., Oller, S., Martinez, X., 2016. Multiscale Computational Homogenization: Review and Proposal of a New Enhanced-First-Order Method. *Archives of Computational Methods in Engineering*, 1–27.
- [39] Saavedra, K., Allix, O., Gosselet, P., 2012. On a multiscale strategy and its optimization for the simulation of combined delamination and buckling. *International Journal for Numerical Methods in Engineering* 91 (7), 772–798.
- [40] Schillinger, D., Harari, I., Hsu, M.-C., Kamensky, D., Stoter, S. K. F., Yu, Y., Zhao, Y., 2016. The non-symmetric Nitsche method for the parameter-free imposition of weak boundary and coupling conditions in immersed finite elements. *Computer Methods in Applied Mechanics and Engineering* 309, 625–652.
- [41] Smit, R. J. M., Brekelmans, W. A. M., Meijer, H. E. H., 1998. Prediction of the mechanical behavior of nonlinear heterogeneous systems by multi-level finite element modeling. *Computer Methods in Applied Mechanics and Engineering* 155 (1), 181–192.
- [42] Terada, K., Hori, M., Kyoya, T., Kikuchi, N., 2000. Simulation of the multi-scale convergence in computational homogenization approaches. *International Journal of Solids and Structures* 37 (16), 2285–2311.
- [43] Terada, K., Kikuchi, N., 2001. A class of general algorithms for multi-scale analyses of heterogeneous media. *Computer Methods in Applied Mechanics and Engineering* 190 (40), 5427–5464.
- [44] Togni, A., Guerich, M., Yvonnet, J., 2016. A multi-scale modeling method for heterogeneous structures without scale separation using a filter-based homogenization scheme. *International Journal for Numerical Methods in Engineering* 108 (1), 3–25.
- [45] van der Sluis, O., Schreurs, P. J. G., Brekelmans, W. A. M., Meijer, H. E. H., 2000. Overall behaviour of heterogeneous elastoviscoplastic materials: Effect of microstructural modelling. *Mechanics of Materials* 32 (8), 449–462.
- [46] Willis, J. R., 1981. Variational and Related Methods for the Overall Properties of Composites. In: Yih, C.-S. (Ed.), *Advances in Applied Mechanics*. Vol. 21. Elsevier, pp. 1–78.

- [47] Willis, J. R., 1983. The Overall Elastic Response of Composite Materials. *Journal of Applied Mechanics* 50 (4b), 1202–1209.
- [48] Yvonnet, J., Bonnet, G., 2014. A consistent nonlocal scheme based on filters for the homogenization of heterogeneous linear materials with non-separated scales. *International Journal of Solids and Structures* 51 (1), 196–209.
- [49] Yvonnet, J., Bonnet, G., 2014. Nonlocal/coarse graining homogenization of linear elastic media with non-separated scales using least-square polynomial filters. *International Journal for Multiscale Computational Engineering* 12 (5), 375–395.